

CONSTRAINING THE ACCRETION FLOW IN SGR A* BY GENERAL RELATIVISTIC DYNAMICAL AND POLARIZED RADIATIVE MODELING

ROMAN V. SHCHERBAKOV¹, ROBERT F. PENNA¹, JONATHAN C. MCKINNEY²

Draft version January 7, 2019

ABSTRACT

The constraints on Sgr A* black hole (BH) and accretion flow parameters are found by fitting polarized sub-mm observations. The observations from 29 papers are averaged into a quasi-quietest set. We run three-dimensional general relativistic magnetohydrodynamical (3D GRMHD) simulations for dimensionless spins $a = 0, 0.5, 0.7, 0.9, 0.98$ till $20000M$, construct an averaged dynamical model, perform GR polarized radiative transfer, and explore the parameter space of spin a , inclination angle θ , position angle (PA), accretion rate \dot{M} , and electron temperature T_e at $6M$ radius. The best-fitting model for spin $a = 0.9$ gives $\chi^2 = 0.99$ with $\theta = 59^\circ$, $\dot{M} = 1.3 \cdot 10^{-8} M_\odot \text{year}^{-1}$, $T_e = 3.2 \cdot 10^{10}$ K at $6M$, the best-fitting model for spin $a = 0.5$ gives $\chi^2 = 0.84$ with $\theta = 70^\circ$, $\dot{M} = 7.0 \cdot 10^{-8} M_\odot \text{year}^{-1}$, and $T_p/T_e = 22$ at $6M$ with $T_e = 3.50 \cdot 10^{10}$ K. We identify the physical phenomena leading to the matched linear polarization (LP), circular polarization (CP), and electric vector position angle (EVPA). Our statistical analysis reveals the most probable spin is $a = 0.9$. The spin $a = 0.5$ solutions are 10 times less probable despite giving lower minimum χ^2 and spin $a = 0$ is excluded as having probability $P(a) < 1\%$. Polarized data allows us to tightly constrain some quantities. Inclination angle, electron temperature, and position angle have ranges $\theta = 59^\circ \pm 9^\circ$, $T_e = 3.4_{-0.9}^{+1.2} \times 10^{10}$ K, and $\text{PA} = 96^\circ \pm 30^\circ$ with 90% confidence. The total range of accretion rate is large, but assuming spin $a = 0.9$ we get $\dot{M}(0.9) = 13_{-3}^{+4} \times 10^{-9} M_\odot \text{year}^{-1}$ interval with 90% confidence. The emission region sizes at 230 GHz of the best-fitting models are found to be marginally consistent with the observed by VLBI technique.

Subject headings: accretion, accretion disks – black hole physics – Galaxy: center – radiative transfer – relativistic processes — polarization

1. INTRODUCTION

Our Galactic Center black hole is one of many inactive galactic cores, the only distinctive feature being its proximity to us. The mass of the black hole (BH) is known to be $M \approx 4.5 \cdot 10^6 M_\odot$ (Ghez et al. 2008) and the spin is uncertain. It resides at a distance of about $d \approx 8.4$ kpc. Because of such proximity, many observations of the source were made in all wavelengths, not completely obscured by absorption: γ -rays, X-rays, IR, (sub-)mm, and radio. The origin of X-rays is bremsstrahlung from the hot gas near the radius of BH gravitational influence (Narayan, Yi & Mahadevan 1995; Narayan et al. 1998; Shcherbakov & Baganoff 2010) and Compton-scattered emission close to the horizon (Moscibrodzka et al. 2009). X-rays at large radius are spatially resolved, which gives an opportunity to test the dynamical models far from the black hole (Shcherbakov & Baganoff 2010). The sub-mm emission is the cyclo-synchrotron originating close to the black hole. The cyclo-synchrotron emission is polarized, both linear and circular polarizations were observed from Sgr A* at several sub-mm wavelengths. The accretion flow was recently resolved at 230 GHz (Doeleman et al.

2008). The GR effects were deemed necessary to explain the small size with full width at half maximum (FWHM) of $37 \mu\text{as}$. The radio emission is also produced by cyclo-synchrotron, but at larger distance from the BH. Thus, to study the effects of GR, one should model sub-mm polarized observations also considering the amount of Compton-scattered X-rays. Modeling the sub-mm in the range 87 GHz to 857 GHz is the goal of the present paper.

First, we need to understand which observations to fit. Sgr A* is a variable source with variability routinely reaching 20% in sub-mm. A popular approach is to fit the simultaneous observations (e.g. Yuan, Quataert & Narayan 2004; Broderick et al. 2009), in particular the set from Falcke et al. (1998). Then, however, two problems arise. The simultaneous observations in a single epoch may not give the representative state of the black hole accretion. For example, monitoring over several years in Zhao et al. (2003) gives the typical flux under 3 Jy at 230 GHz and the observation of $F_\nu > 3$ Jy in Falcke et al. (1998) may represent a flare. Another problem is that one cannot easily combine two sets of observations in such an approach: the addition of a new frequency would require redoing observations of every other frequency at that instant of time. It is more reasonable to consider the statistics of observations and find the typical values of quantities at each frequency. At the highest sub-mm frequency and harder wavelengths the flux can flare several times over the typical level, so we calculate the median values of quantities, instead of

rshcherbakov@cfa.harvard.edu

¹ <http://www.cfa.harvard.edu/%7Ershcherb/rpenna@cfa.harvard.edu>

Harvard-Smithsonian Center for Astrophysics, 60 Garden Street, Cambridge, MA 02138, USA

² jmckinne@stanford.edu

Department of Physics and Kavli Institute for Particle Astrophysics and Cosmology, Stanford University, Stanford, CA 94305-4060, USA; Chandra Fellow

the mean ones. The mean fluxes may not fully represent the typical “quiescent” state.

A good GR dynamical model of accretion is required to reproduce the observations. The population of models grew into a quite colorful zoo over the years: advection-dominated accretion flow (ADAF) (Narayan & Yi 1995), advection-dominated inflow-outflow solution (ADIOS) (Blandford & Begelman 1999), jet-ADAF (Yuan, Markoff, & Falcke 2002), jet (Maitra, Markoff & Falcke 2009), and the models directly based on numerical simulations. The analytic models in general have more free parameters and also incorporate many assumptions (Huang et al. 2008, 2009a), making their use an unreliable enterprise. The numerical simulations require fewer inputs and settle into a quasi-steady accretion, which justifies their use. General relativistic magnetohydrodynamical (GRMHD) simulations, like those performed in McKinney & Gammie (2004); McKinney & Blandford (2009); Penna et al. (2010), are necessary for modeling matter infall onto a rotating BH since magnetohydrodynamical (MHD) simulations require a quasi-Newtonian potential that inaccurately models the effective potential (Ghosh & Mukhopadhyay 2007). The behavior of accretion is also different between the two-dimensional and the three-dimensional models (Igumenshchev 2008) such as due to Cowling’s anti-dynamo theorem, so we model the flow in three dimensions. Numerical simulations, like we perform, are limited to a region relatively close to the BH (Dexter et al. 2009; Moscibrodzka et al. 2009), whereas emission and Faraday rotation come from regions far from the BH. Thus, we analytically extend the modeled region out to $20000M$, do radiative transfer and find the best fit to data. The extension to large radius also allows to define the electron temperature more consistently (Sharma et al. 2007).

The good dynamical model does not eliminate all the uncertainty of comparing to data. Indeed, a proper treatment of radiation and statistical analysis rely crucially upon estimating the uncertainties. The simplest Newtonian radiation consideration (Yuan, Quataert & Narayan 2004) does not provide a means to treat radiation close to the BH. A quasi-Newtonian approach offers some improvement (Goldston, Quataert & Igumenshchev 2005; Chan et al. 2009). The general relativistic treatment of unpolarized light (Fuerst & Wu 2004; Dexter et al. 2009; Dolence et al. 2009) captures most GR effects, but only polarized general relativistic radiative transfer (Broderick et al. 2009; Gammie & Leung 2010; Shcherbakov & Huang 2010) is exact and captures all GR phenomena. The present paper adopts this latest approach. We are able to compare the results of modeling to extensive polarization data, constraining much better the flow parameters and spin. In fact, fitting only the total flux spectrum does not constrain the spin. The values from $a = 0$ (Broderick et al. 2009) to $a = 0.9$ (Moscibrodzka et al. 2009) are found in the literature. Other radiation ingredients may include Comptonization (Moscibrodzka et al. 2009) and radiation from non-thermal electrons (Mahadevan 1998; Özel, Psaltis & Narayan 2000; Yuan, Quataert & Narayan 2004). We do not consider

non-thermal electrons, but find that strong radio emission comes from the polar regions of the flow even with thermal electrons. The emissivities are calculated in synchrotron approximation (Legg & Westfold 1968; Sazonov 1969; Pacholczyk 1970; Melrose 1971) with exact thermal electron distribution. The emissivities in synchrotron approximation are very close to the exact cyclo-synchrotron emissivities (Leung, Gammie & Noble 2009; Shcherbakov & Huang 2010), so we use the former. However, the exact Faraday rotation and conversion expressions are employed (Shcherbakov 2008) as no similar approximations exist for them.

The comparison of simulations to observations is a non-trivial task. One needs to start with computing the allowed differences, the “errors”, of the measured quantities from the observed ones. The observation “errors” of Sgr A* are normally small compared to the intrinsic source variability. Thus, we can assume the variability of the observed quantities to give the “errors” and calculate the correspondent χ^2 . The χ^2 -based statistical analysis should first prove there are regions in the parameter space with $\chi^2 \sim 1$. Then the probability density ρ should be integrated over the entire parameter space and the expectation values of model parameters should be found together with the uncertainties. The full statistical analysis is performed in the present work.

The paper is constructed as follows. We summarize the observational manifestations of accretion flow in sub-mm in § 2. The 3D GRMHD simulations are described in § 3 together with the analytic extension to large radii and electron heating prescription. We run simulations for dimensionless spins $a = 0, 0.5, 0.7, 0.9, 0.98$. The GR polarized radiative transfer is elaborated upon in § 4. The statistical analysis technique is presented in § 5. We compute the intrinsic variability of the observed and simulated quantities, define the effective errors and find χ^2 for statistical analysis. The set of observations considered includes the spectral energy distribution (SED) within 87 GHz to 857 GHz frequency range, linear polarization (LP) fractions at 87 GHz, 230 GHz and 349 GHz, and circular polarization (CP) fractions at 230 GHz and 349 GHz. The parameter space incorporates spin a , inclination angle θ , accretion rate \dot{M} , and the ratio of proton to electron temperatures T_p/T_e at $6M$ from the center. In § 6 we discuss the numerous results: best fits to observations, behaviors of χ^2 near the best fits, the importance of various physical effects in producing CP, LP, and electric vector position angle (EVPA), probability densities for spins marginalized over the model parameters, expectation values of quantities, image size estimates, and the actual images of total and polarized intensities. We use geometrized units such that the speed of light and gravitational constant are unity.

Two good fits to observations are found with $\chi^2 \approx 1$ for different spins. The best fit for spin $a = 0.9$ has $\theta = 59^\circ$, $\dot{M} = 1.3 \cdot 10^{-9} M_\odot \text{year}^{-1}$, and $T_p/T_e = 23.5$ at $6M$, the best fit for spin $a = 0.5$ has $\theta = 70^\circ$, $\dot{M} = 7.0 \cdot 10^{-8} M_\odot \text{year}^{-1}$, and $T_p/T_e = 22$ at $6M$. Spin $a = 0$ is excluded as having a low integrated probability $P(a)$, but all other spins are possible. Spin $a = 0.9$ shows the highest $P(a)$ with probability for spin $a = 0.5$ being 10 times lower. The 90% confidence intervals for the inclination angle, electron temperature, and spin position angle are

$\theta = 59^\circ \pm 9^\circ$, $T_e = 3.4_{-0.9}^{+1.2} \times 10^{10}$ K, and $\text{PA} = 96^\circ \pm 30^\circ$. The total range of accretion rates is wide, but assuming spin $a = 0.9$ we get $\dot{M}(0.9) = 13_{-3}^{+4} \times 10^{-9} M_\odot \text{year}^{-1}$ with 90% confidence intervals. We do not calculate the expectation values for the spin or accretion rate, since the dispersion of their values is too large. The discussion in § 7 compares these results to previous estimates, emphasizes the significance of polarization, notes the sources of errors, requests for specific observations, and outlines prospects for future work. We note that fitting only the total flux provides very loose constraints on spin, inclination angle or accretion rate.

2. OBSERVATIONS

Sgr A* is known to be a highly variable source, yet quiescent models of Sgr A* emission are popular and useful. Thus, a proper definition of quiescent quantities is required from observations. The so-called “quiescent” lightcurves were modeled by Yuan, Quataert & Narayan (2004); Broderick et al. (2009). However, both papers summarize a limited set of observations and do not perform any averaging. The sub-mm fluxes reported in Yuan, Quataert & Narayan (2004) essentially consist of an old short set of observations (Falcke et al. 1998) and partial SMA data (Zhao et al. 2003). Broderick et al. (2009) adds to that the rest of SMA data (Marrone et al. 2006a,b, 2007, 2008). Thus, only 6 out of at least 29 papers on sub-mm observations of Sgr A* were employed. Our work is improved compared to these papers by computing a quasi-quiescent spectrum based on all papers to date reporting sub-mm observations of Sgr A*.

The kinds of reported observations vary greatly in a covered period from several hours (An et al. 2005) to several years (Krichbaum et al. 2006). We take the median values from each paper. The data from close frequencies are bunched to produce a single SED point. Then the median is found for each frequency over all papers, weighing longer periods more. The mean frequency is ascribed to each group. Reports of observations over several months are ascribed weight 8, over weeks — 4, over days — 2, and observations within a day have weight 1. In case the paper reports measurements on a set of timescales, we only consider the longest period results to eliminate the reporting bias towards flares. There are some unreliable observations over the set of papers. Often the unreliable data is produced by observing in sub-mm with large beam size and being contaminated by dust and other sources. For example, SMT data (Yusef-Zadeh et al. 2009), early CSO measurements (Serabyn et al. 1997), and early JCMT measurements (Aitken et al. 2000) have problems. We exclude these data in quiescent spectrum calculations. The interferometric observations, especially with VLBI, help to reduce an error of otherwise unreliable observations, e.g. with BIMA array (Bower et al. 2001). However, some inconsistencies still exist of simultaneous observations at the same frequency with different instruments (Yusef-Zadeh et al. 2009). We summarize observations in Table 1. The sets of close frequencies are bunched into 11 groups, excluding papers with frequencies far from the center of each group. In particular, the 94 GHz and 95 GHz observations in Li et al. (2008); Falcke et al. (1998) and the 112 GHz observations in Bower et al. (2001) are excluded. The CP fractions of -1.2% at

230 GHz and -1.5% at 349 GHz are based on preliminary reports from SMA collaboration. We do not incorporate the source size measurements (Doeleman et al. 2008) in calculating the χ^2 , but check that the best fit model is consistent with those observations.

Figure 1 shows the compilation of the quiescent spectrum. The data are represented by two lines and the shaded area in between. The upper (lower) line is the median of the results reported in different papers plus (minus) the median absolute deviation (MAD), found either directly from observations, or, when the observations do not provide a representative sample, from simulations. We will discuss this point in more details in the statistical analysis section (§ 5). The red curve on F_ν plot represents the analytic fit $F_\nu = 0.295\nu^{0.4} \exp(-(\nu/1300)^2)$, where flux is in Jy and frequency is in GHz. The light points on F_ν plot show the spectrum in Broderick et al. (2009), the light points on $LP\%$ plot represent the incomplete compilation of Bower et al. (1999b); Macquart et al. (2006); Marrone et al. (2007). The EVPA angle is not included into the fitting procedure and we do not calculate the MAD for it.

3. 3D GRMHD SIMULATIONS AND DYNAMICAL MODEL

The key to producing a model with few free parameters lies in simulating the physical system in full GR. Even limited GR simulations have significantly improved our understanding in the recent past. It is now possible to simulate a radiatively inefficient accretion flow in full GR with fully conservative MHD numerical scheme (Gammie et al. 2003) and successfully complete the convergence tests with changing resolution (Shafee et al. 2008). Such simulations are run until the accretion flow reaches a quasi-steady state out to the large distance from the rotating Kerr BH. We are employing a set of such simulations.

The setup of our simulations is identical to that in Penna et al. (2010) unless stated otherwise. Briefly stated, the initial configuration of the flow constitutes an isentropic equilibrium torus aligned with the spin axis (De Villiers, Hawley & Krolik 2003). The initial magnetic field consists of several poloidal loops in the torus with a minimum plasma β of about 100. The magnetic field gets amplified by the magneto-rotational instability (MRI) and transports angular momentum out and matter into the BH. The study considers a set of non-cooling disks with dimensionless spin parameter $a = 0, 0.5, 0.7, 0.9, 0.98$. All models have an initial inner torus edge at $r_{\text{in}} = 20M$ and a torus pressure maximum at $R_{\text{max}} = 65M$ for uniformity. We employ HARM 3D code (Gammie et al. 2003) in horizon-penetrating coordinates. Our grid is uniform in azimuthal angle ϕ and a π wedge is simulated instead of full 2π domain to increase the speed. The radial grid mapping is close to logarithmic. It is represented by

$$r(x^{(1)}) = R_0 + \exp(x^{(1)}), \quad (1)$$

where $R_0 = 0.3M$ and $x^{(1)}$ is uniform. Out of 256 radial grid cells, several lie inside the BH horizon, ensuring no causal connection between the artificial boundary condition inside the horizon and the flow outside the horizon.

Table 1
Summary of Polarization Observations

ν [GHz]	Telescopes	F_ν [Jy]	LP [%]	CP [%]	EVPA [°]
8.45	VLA	0.69 (Serabyn et al. 1997; Falcke et al. 1998; Bower et al. 1999a; An et al. 2005)	...	-0.25 (Bower et al. 1999a)	
14.90	VLBA, VLA	0.90 (Serabyn et al. 1997; Falcke et al. 1998; Bower et al. 2002; Herrnstein et al. 2004; An et al. 2005; Yusef-Zadeh et al. 2009)	...	-0.62 (Bower et al. 2002)	...
22.50	VLBA, VLA	1.07 (Serabyn et al. 1997; Falcke et al. 1998; Bower et al. 1999b; Herrnstein et al. 2004; An et al. 2005; Lu et al. 2008; Yusef-Zadeh et al. 2007, 2009)	0.19 (Bower et al. 1999b; Yusef-Zadeh et al. 2007)
43	GMVA, VLBA, VLA	1.16 (Falcke et al. 1998; Lo et al. 1998; Bower et al. 1999b; Herrnstein et al. 2004; An et al. 2005; Shen et al. 2005; Krichbaum et al. 2006; Yusef-Zadeh et al. 2007; Lu et al. 2008; Yusef-Zadeh et al. 2009)	0.50 (Bower et al. 1999b; Yusef-Zadeh et al. 2007)
88	BIMA, MPIFR, VLBA, VLA, Nobeyama, NMA, CARMA	1.58 (Falcke et al. 1998; Krichbaum et al. 1998; Bower et al. 1999b; Doeleman et al. 2001; Miyazaki et al. 2004; Shen et al. 2005; Krichbaum et al. 2006; Macquart et al. 2006; Lu et al. 2008; Yusef-Zadeh et al. 2009)	1.11 (Bower et al. 1999b; Macquart et al. 2006)	...	103 (Bower et al. 1999b; Shen et al. 2005; Macquart et al. 2006)
102	OVRO, CSO-JCMT, Nobeyama, NMA, IRAM	1.42 (Serabyn et al. 1997; Falcke et al. 1998; Miyazaki et al. 2004; Mauerhan et al. 2005; Yusef-Zadeh et al. 2009)
145	Nobeyama, NMA, IRAM, JCMT	2.25 (Falcke et al. 1998; Aitken et al. 2000; Miyazaki et al. 2004; Yusef-Zadeh et al. 2009)
230	IRAM, JCMT, BIMA, SMA, OVRO	2.18 (Serabyn et al. 1997; Falcke et al. 1998; Aitken et al. 2000; Bower et al. 2003, 2005; Zhao et al. 2003; Krichbaum et al. 2006; Marrone et al. 2006a, 2007, 2008; Doeleman et al. 2008; Yusef-Zadeh et al. 2009)	7.61 (Bower et al. 2003, 2005; Marrone et al. 2007, 2008)	-1.2 (Munoz et al. (2009), Munoz et al. 2010, in prep.)	117 (Bower et al. 2003, 2005; Marrone et al. 2007, 2008)
349	SMA, CSO, JCMT	3.07 (Aitken et al. 2000; An et al. 2005; Marrone et al. 2006b, 2007, 2008; Yusef-Zadeh et al. 2009)	7.03 (Marrone et al. 2006b, 2007)	-1.5 (Munoz et al. 2010, in prep.)	146 (Marrone et al. 2006b, 2007)
674	CSO, SMA	3.20 (Marrone et al. 2006a, 2008; Yusef-Zadeh et al. 2009)
857	CSO	2.79 (Serabyn et al. 1997; Marrone et al. 2008; Yusef-Zadeh et al. 2009)

The θ -grid mapping is

$$\theta(x^{(2)}) = \left[Y(2x^{(2)} - 1) + (1 - Y)(2x^{(2)} - 1)^7 + 1 \right] \frac{\pi}{2} \quad (2)$$

between 0 and π for uniform $x^{(2)}$ and $Y = 0.65$. The resolution of simulations is $N_r \times N_\theta \times N_\phi = 256 \times 64 \times 32$. We run the simulations till $20000M$. The accretion rate settles to roughly a constant at about $6000M$ at radii up to $25M$, whereas the magnetic field does not settle until about $14000M$. We use the $14000M - 20000M$ time range to approximate the true steady-state for the non-cooling accretion flow out to about a radius of $25M$. We employ the averaged dynamical model for the purpose of analyzing the whole model parameter space. It is not computationally viable to surf the parameter space, calculating the averages over the series of simulation time shots. The average model incorporates the direct temporal averages at each coordinate point of electron number density n_e , velocity u^α , and energy density U . The averaging of magnetic field is performed at each point in the co-moving locally flat reference frame. The square-averaged \mathbf{B} is used to calculate plasma emissivities and Faraday conversion, since emissivities are dependent on

the typical value of B , and Faraday conversion depends on B^2 . In turn the arithmetic mean is better suited for Faraday rotation, since it depends on vector \mathbf{B} . For simplicity the square-averaged $\langle \mathbf{B}^2 \rangle^{0.5}$ is ascribed the direction of the averaged \mathbf{B} . Figure 2 shows matter stream lines as vectors and number density n_e as greyscale map. The large scale vortices existing on a single time shot (panel (a)) almost disappear, when averaged over $6000M$ (panel (b)) in between $14000M$ and $20000M$. The density is the highest in the equatorial plane on average, but deviations are present on the instantaneous map. The innermost stable circular orbit (ISCO) does not have any special significance: density and internal energy density increase through ISCO towards the black hole horizon. Figure 3 shows magnetic field lines as vectors and comoving electromagnetic energy density $\propto B^2$ as a greyscale map. The structure of magnetic field at early times remembers the initial multi-loop field geometry (Penna et al. 2010), but switches to a split-monopole configuration at late times. Such switching of magnetic field configuration suggests that the final split-monopole field is universal, which would not be obvious, if we were to start with a split monopole. The magnetic field struc-

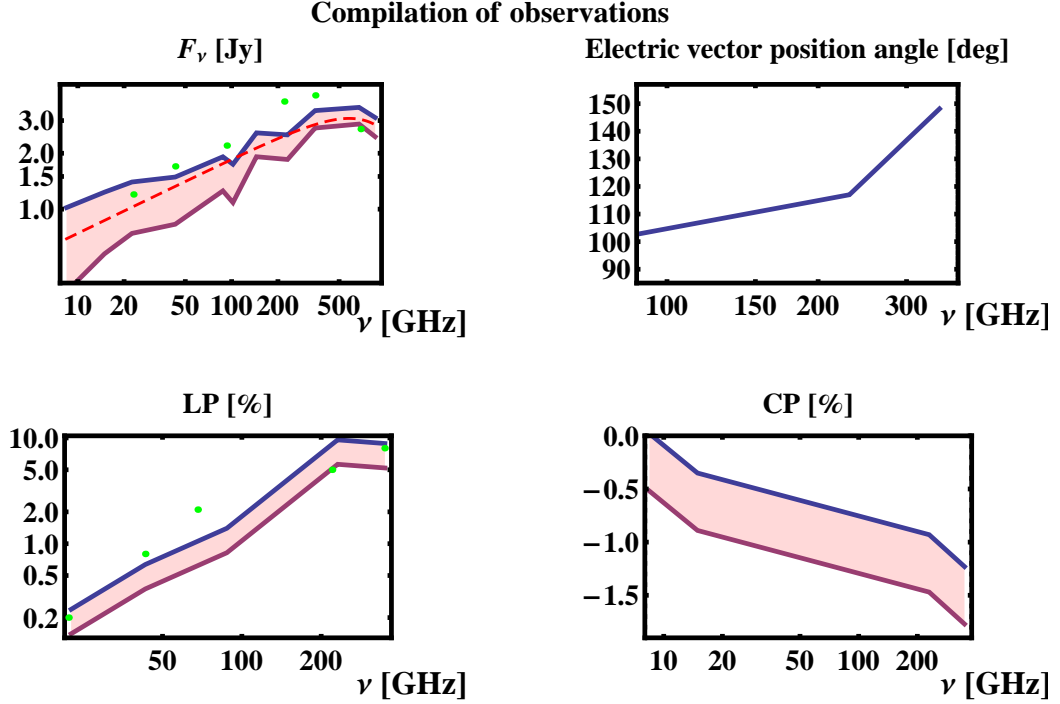


Figure 1. Average SEDs of specific flux F_ν , linear polarization (LP) fraction, electric vector position angle (EVPA), and circular polarization (CP) fraction. The upper and lower curves show the average quantities plus/minus the characteristic variability. The shaded area designates the range. Green points show previously compiled data (Broderick et al. 2009), dashed line on F_ν plot represents the analytic approximation $F_\nu(Jy) = 0.295\nu^{0.4} \exp(-(\nu/1300)^2)$ for frequency ν in GHz.

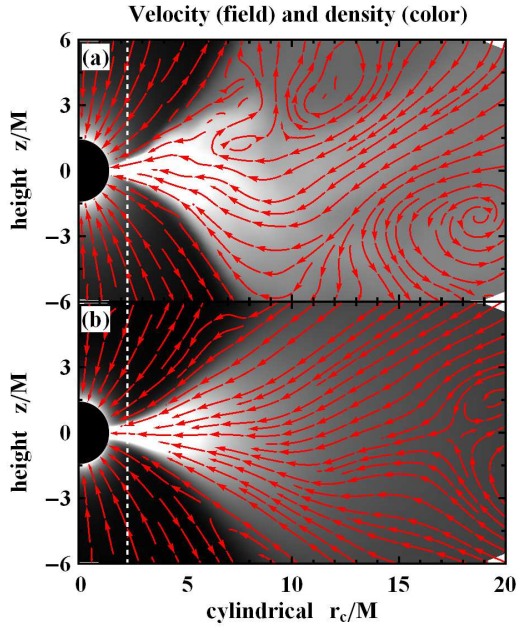


Figure 2. Stream lines of velocity (red vectors) and number density n_e (greyscale map) for spin $a = 0.9$ in the meridional plane: single timeshot at $t = 14000M$ on the upper (a) panel and time average between $t = 14000M$ and $t = 20000M$ on the lower (b) panel.

ture of a single time shot (panel (a)) looks quite similar to the structure of the average between 14000M and 20000M (panel (b)). The polar region of the flow has the strongest magnetic field.

The grid points in θ (eq. 2) are concentrated near the

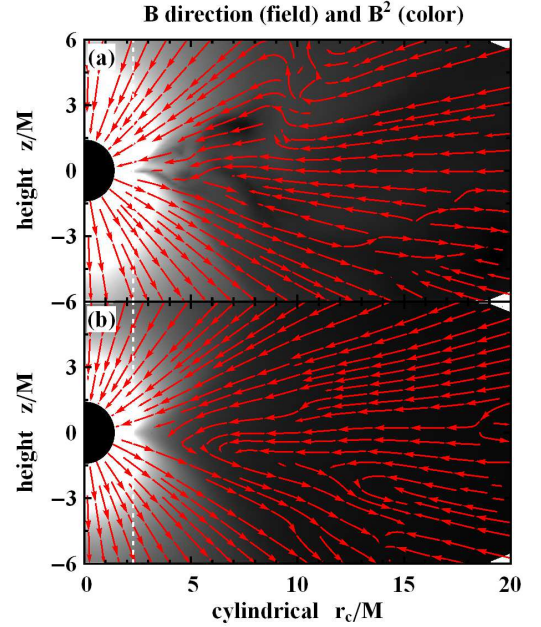


Figure 3. Magnetic field lines (red vectors) and comoving electromagnetic energy density $\propto B^2$ (greyscale map) for spin $a = 0.9$ in the meridional plane: single timeshot at $t = 14000M$ on the upper (a) panel and time average between $t = 14000M$ and $t = 20000M$ on the lower (b) panel.

equator to reliably resolve the MRI. The resolution in the polar region is poor, which leads to very efficient energy dissipation there and fast heating of corona. Such overheated corona seems unphysical (see discussion in McKinney 2006; Penna et al. 2010). Moreover, the re-

sults of GR radiative transfer suggest that the overheated strongly magnetized corona produces significant emission in sub-mm waveband that would cause an overshoot in the size constraints of the emitting region. The numerical fix for this problem consists of setting the “floor:” upper limit on magnetization $B^2/(4\pi\rho) \leq 10$. The stability of the numerical code also requires setting an upper limit on energy density U as $B^2/(4\pi U) \leq 100$ and $U/\rho \leq 10$.

The flow is evolved in a quasi-steady state for $6000M$ from $14000M$ till $20000M$, which corresponds to 8 orbits at $r = 25M$. The flow is not sufficiently settled at larger radii, however, substantial Faraday rotation happens and some emission occurs outside $25M$, which requires that we extend the dynamical model to larger radii $r > 25M$. The profiles of number density n_e , internal energy density U , magnetic field B and velocity v are extended as power-laws up to $r = 20000M$. The relevant power-law is obtained for number density by matching the known value $n_e = 130\text{cm}^{-3}$ at about $1.5'' \approx 3 \cdot 10^5 M$ (Baganoff et al. 2003). The small differences from the revised later estimates in Shcherbakov & Baganoff (2010) are unimportant for our purposes. The profile of magnetic field is extended smoothly and the profile of velocity is determined from mass conservation. It is less trivial to extend the energy density and compute the proton and electron temperatures.

Neither T_p nor T_e are given directly by the simulation. However, it is crucial to know the electron temperature T_e to determine the emission. Our solution is to split the total energy density U , given by the simulation results, between the proton temperature T_p and the electron temperature T_e . The energy balance states

$$\frac{U}{\rho} = c_p k_B T_p + c_e k_B T_e, \quad (3)$$

where $c_p = 3/2$ and $c_e \geq 3/2$ are the respective heat capacities, ρ is the rest-mass density, and k_B is Boltzmann constant. The difference of temperatures $T_p - T_e$ is influenced by three effects: equilibration by Coulomb collisions at large radii, difference in heating rates f_p and f_e of protons and electrons operating at intermediate radii, and difference in heat capacities operating close to the BH. All the effects can be incorporated into an equation as

$$v_r \frac{d(T_p - T_e)}{dr} = -\nu_c (T_p - T_e) + \left(\frac{1}{c_p} \frac{f_p}{f_p + f_e} - \frac{1}{c'_e} \frac{f_e}{f_p + f_e} \right) v_r \frac{d(U/\rho)}{k_B dr}, \quad (4)$$

where

$$\nu_c = 8.9 \cdot 10^{-11} \left(\frac{T_e}{3 \cdot 10^{10}} \right)^{-3/2} \frac{n_e}{10^7} \quad (5)$$

is the non-relativistic temperature equilibration rate by collisions (Shkarofsky et al. 1966), all quantities being measured in CGS units. We consider protons to always have non-relativistic heat capacity and collisions to always obey the non-relativistic formula. The magnitudes of errors introduced by these simplification are negligible. The exact expressions for total electron heat capacity and

differential heat capacity are approximated as

$$c_e = \frac{U_e/\rho}{k_B T_e} \approx \frac{3}{2} \frac{0.7 + 2\theta_e}{0.7 + \theta_e}, \quad (6)$$

$$c'_e = \frac{d(U_e/\rho)}{k_B dT_e} \approx 3 - \frac{0.735}{(0.7 + \theta_e)^2} \quad (7)$$

correspondingly with the error $< 1.3\%$, where

$$\theta_e = \frac{k_B T_e}{m_e c^2} \quad (8)$$

is the dimensionless electron temperature. It was recently shown (Sharma et al. 2007) that the ratio of heating rates in non-relativistic regime in a disk can be approximated as

$$\frac{f_e}{f_p} = C \sqrt{\frac{T_e}{T_p}} \quad (9)$$

with a constant C . This formula is adopted in the relativistic regime as well, since no better prescription is available. Sharma et al. (2007) found the value $C = 0.34 - 0.35$ in simulations, whereas we find $C = 0.34 - 0.35$ for the best-fitting models (see § 6). The agreement may not be purely coincidental and may to some extent justify the prescription chosen. The proton and electron temperatures are determined at each point in the following way. We first take a late-time part of a simulation with spin a . Then we compute the average profiles of radial velocity v_r , number density n_e , and U/ρ near the equatorial plane, extend them to the outer boundary at $r_{\text{out}} = 3 \cdot 10^5 M$ as discussed above and solve the equations (3,4) from r_{out} down to the inner grid cell point. The temperatures are set to $T_e = T_p = 1.5 \cdot 10^7$ K at r_{out} (Baganoff et al. 2003; Shcherbakov & Baganoff 2010). On the next step we make a correspondence of the values of U/ρ to the calculated T_e and T_p . At each point of the simulation, even not on the equator, we draw temperatures from this correspondence. The typical profiles of proton and electron temperatures are shown in Figure 4. The temperatures stay equal till $\sim 10^4 M$ due to collisions despite different heating prescriptions. Within $3 \cdot 10^3 M$ the timescale of collisional equilibration becomes relatively long and electrons become relativistic, thus T_e diverges down from T_p . The slopes of curves inside and outside $25M$ are slightly different, which emphasizes the limitations of numerical simulations.

For a given accretion rate there exists a unique dependence of the ratio of temperatures T_p/T_e at $6M$ on the heating constant C . Thus, the reference to the “temperature of the model” means the ratio of temperatures T_p/T_e at $6M$ or the correspondent heating constant C . We commonly use the former quantity as the more visual one.

4. GR POLARIZED RADIATIVE TRANSFER

General relativistic polarized radiative transfer is the essential tool of converting the dynamical model of an accretion flow into the set of observable quantities (Broderick et al. 2009; Gammie & Leung 2010; Shcherbakov & Huang 2010). We closely follow Shcherbakov & Huang (2010) for the transfer technique. Similarly to Huang et al. (2009a), we define the polarized basis in the picture plane, where one vector points North,

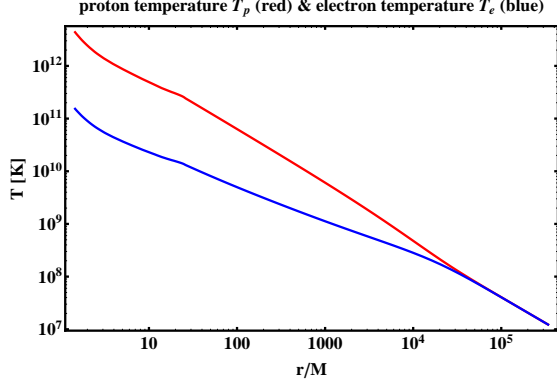


Figure 4. The temperatures of protons T_p (upper red line) and electrons T_e (lower blue line) as functions of radius for heating parameter $C = 0.345$ and accretion rate $\dot{M} = 1.2 \cdot 10^{-8} M_\odot \text{ year}^{-1}$, which leads to $T_p/T_e = 23$ and $T_e = 3.2 \cdot 10^{10} \text{ K}$ at $r = 6M$. The dynamical model with this heating prescription, this accretion rate, and spin $a = 0.9$ fits well the polarization observations (see § 6).

another vector points East, and the wavevector points towards the observer. We parallel transport this basis in the direction of the black hole and do the radiative transfer along the ray in the opposite direction. At each point along the ray we go to the locally-flat co-moving reference frame, calculate the angles between magnetic field and the basis vectors, and compute the Faraday conversion, Faraday rotation, emissivities, and absorptivities. This approach appears to be not harder computationally compared to the covariant calculation of angles without the locally-flat co-moving frame (Broderick et al. 2009; Huang et al. 2009a).

The only difference from Shcherbakov & Huang (2010) is in our calculations of plasma response. That paper offered the way to find exactly the emissivities, absorptivities, Faraday rotation, and conversion coefficients for thermal and other isotropic particle distributions. For simplicity, we employ the fitting formulas for Faraday rotation and Faraday conversion and synchrotron approximation for emissivities in thermal plasma. We define

$$X = \frac{2}{3} \frac{\nu}{\nu_B \gamma^2 \sin \theta_B}, \quad (10)$$

where θ_B is $\mathbf{k}\text{-}\mathbf{B}$ angle, γ is electron gamma factor, and $\nu_B = eB/(2\pi m_e c)$ is the cyclotron frequency. Then following (Legg & Westfold 1968; Melrose 1971), we write down emissivities in I, Q, and V modes as

$$\begin{aligned} \varepsilon_I &= \frac{\sqrt{3}}{2} \frac{e^2}{c} \nu_B \sin \theta_B \int_1^{+\infty} d\gamma N(\gamma) X \int_X^{+\infty} dz K_{5/3}(z), \\ \varepsilon_Q &= \frac{\sqrt{3}}{2} \frac{e^2}{c} \nu_B \sin \theta_B \int_1^{+\infty} d\gamma N(\gamma) X K_{2/3}(X), \\ \varepsilon_V &= \frac{2}{\sqrt{3}} \frac{e^2}{c} \nu_B \cos \theta_B \int_1^{+\infty} d\gamma \frac{N(\gamma)}{\gamma} \times \\ &\quad \times \left[X K_{1/3}(X) + \int_X^{+\infty} dz K_{1/3}(z) \right]. \end{aligned} \quad (11)$$

Here $K_z(x)$ is the Bessel function of the 2-nd kind of order z . We employed IEEE/IAU definitions of Stokes Q , U , and V (Hamaker & Bregman 1996), also chosen in Shcherbakov & Huang (2010): counter-clockwise

rotation of electric field as seen by the observer corresponds to positive $V > 0$. Under this definition the sign of V emissivity (11) is the opposite to that in standard theoretical textbooks (Rybicki & Lightman 1967). A variation of emissivity formulas (10,11) exists: Sazonov (1969); Pacholczyk (1970) effectively define $X = 2\nu/(3\nu_B(\gamma-1)^2 \sin \theta_B)$, integrating over particle energy instead of γ . This approximation appears to give significantly higher errors at low particle energies.

Next, one needs to specify which $N(\gamma)$ to use. Various $N(\gamma)$ correspond to several synchrotron approximations for thermal plasmas. The ultrarelativistic approximation (Pacholczyk 1970; Huang et al. 2009a) $N(\gamma) = \exp(-(\gamma-1)/\theta_e)(\gamma-1)^2/2/\theta_e^3$ gives the simplest distribution. However, the exact thermal distribution of particles

$$N(\gamma) = \gamma \sqrt{\gamma^2 - 1} \frac{\exp(-\gamma/\theta_e)}{\theta_e K_2(\theta_e^{-1})} \quad (12)$$

allows for more precise computation of radiation. Synchrotron emissivities based on the equations (10,11) with the exact thermal distribution (12) agree with the exact cyclo-synchrotron emissivities ε_I , ε_Q , and ε_V (Leung, Gammie & Noble 2009; Shcherbakov & Huang 2010) to within 2% for typical dynamical models and frequencies $> 100 \text{ GHz}$. The emissivities integrated over the ultrarelativistic thermal distribution normally have $\sim 10\%$ error.

The thermal absorptivities are found from emissivities (11) via Kirchhoff's law

$$\alpha_{I,Q,V} = \varepsilon_{I,Q,V}/S_\nu, \quad (13)$$

where $S_\nu = 2k_B T_e \nu^2/c^2$ is the source function for low photon energies $h\nu \ll k_B T_e$. The Faraday rotation ρ_V and Faraday conversion ρ_Q coefficients are taken from (Shcherbakov 2008):

$$\begin{aligned} \rho_V &= g(Z) \frac{2n_e e^2 \nu_B}{m_e c \nu^2} \frac{K_0(\theta_e^{-1})}{K_2(\theta_e^{-1})} \cos \theta, \\ \rho_Q &= f(Z) \frac{n_e e^2 \nu_B^2}{m_e c \nu^3} \left[\frac{K_1(\theta_e^{-1})}{K_2(\theta_e^{-1})} + 6\theta_e \right] \sin^2 \theta. \end{aligned} \quad (14)$$

Here

$$Z = \theta_e \sqrt{\sqrt{2} \sin \theta \left(10^3 \frac{\nu_B}{\nu} \right)} \quad (15)$$

and

$$\begin{aligned} g(Z) &= 1 - 0.11 \ln(1 + 0.035Z), \\ f(Z) &= 2.011 \exp\left(-\frac{Z^{1.035}}{4.7}\right) - \\ &\quad - \cos\left(\frac{Z}{2}\right) \exp\left(-\frac{Z^{1.2}}{2.73}\right) - 0.011 \exp\left(-\frac{Z}{47.2}\right) \end{aligned} \quad (16)$$

are the fitting formulas for deviation of ρ_V and ρ_Q from analytic results for finite ratio ν_B/ν . The deviation of $f(Z)$ from 1 is significant for the set of observed frequencies ν , temperatures θ_e , and magnetic fields found in the typical models of Sgr A*. These formulas constitute a good fit to the exact result for the typical parameters of the dynamical model.

With all sophisticated pieces of physics being incorporated into the model, the speed of the numerical code be-

comes an essential constraint. Polarized radiative transfer can take much longer to perform compared to the non-polarized radiative transfer when using an explicit integration scheme to evolve the Stokes occupation numbers N_Q , N_U , and N_V . A large Faraday rotation measure and Faraday conversion measure lead to oscillations between those quantities. One of the solutions is to use an implicit integration scheme, while another solution is to do a substitution of variables. In the simple case of Faraday rotation leading to interchange of N_Q and N_U , the obvious choice of variables is the amplitude of oscillations and the phase. Thus the cylindrical polarized coordinates arise

$$\begin{aligned} N_Q &= N_{QU} \cos \phi, \\ N_U &= N_{QU} \sin \phi. \end{aligned} \quad (17)$$

Then the amplitude N_{QU} slowly changes along the ray and the angle ϕ changes linearly, which gives an improvement in speed. In the presence of substantial Faraday conversion, the polarization vector precesses along some axis in Poincaré sphere, adding an interchange of circularly and linearly polarized light. The polar polarized coordinates would be more suitable in this case:

$$\begin{aligned} N_Q &= N_{\text{pol}} \cos \phi \sin \psi, \\ N_U &= N_{\text{pol}} \sin \phi \sin \psi, \\ N_V &= N_{\text{pol}} \cos \psi, \end{aligned} \quad (18)$$

where N_{pol} is the total polarized intensity, the change of ϕ angle is mainly due to Faraday rotation and ψ angle changes owing to Faraday conversion. The application of this technique speeds up the code exponentially at low frequencies $\nu < 100$ GHz.

Besides improving the code, we perform a number of convergence tests to make sure the final intensities are correct to at least 1%. We use a uniform grid in the picture plane with N points in each dimension. Even though, for a single timeshot, $N = 400$ (Dexter et al. 2009) maybe a better number to use, $N = 85$ works well for the averaged smooth model. The size of the integration domain is chosen individually for each frequency and a unique set of geodesics is constructed for each frequency. Another essential parameter is the distance from the BH where the integration starts. The dependence of synchrotron emissivity on temperature and magnetic field strength is so strong that it negates the effect of gravitational redshift close to the BH. The accuracy of 1% is achieved in sub-mm for computation out from $1.01r_H$, where r_H is the horizon radius.

5. STATISTICAL ANALYSIS

The statistical analysis is a necessary tool to compare the model predictions to observations and to discriminate between models. However, it has only recently been first applied to the Galactic Center accretion (Dexter et al. 2009; Broderick et al. 2009; Shcherbakov & Baganoff 2010). When the number of model parameters is large (Huang et al. 2009a) or the variety of considered observations is small (Moscibrodzka et al. 2009), it is possible to find an exact fit to the data or say that for some model parameters the fit does not exist. As we consider the broad range of observations, we do the full statistical analysis.

We want to probe our models with the test on equality of means of two distributions, one being generated by observations and another by simulations. It is called Student's t-test for normally distributed quantities. We would need to apply the test for each observable at each frequency and find the probability density that the observed quantity is consistent with the simulated quantity. The probability densities are then multiplied assuming independence of the observables. To do the analysis, we could assume a normal distribution of individual quantities and employ t-distribution of the sequence with error $\sigma = \sqrt{\sigma_1^2/n_1 + \sigma_2^2/n_2}$, where σ_1 and σ_2 are the standard deviations of the observational sequence and the synthesized sequence correspondingly and n_1 and n_2 are sequence lengths. As we are fitting the observables from an averaged profile, there is no statistics from simulations. We assume that the radiative transfer on the top of the averaged profile represents well the average of radiative transfers over many time shots and $\sigma_2 = 0$. Then, the typical number of representative observations is $n_1 \sim 3$, thus $\sigma \sim 0.6\sigma_1$. This typical error is on the order of median deviation $MAD \approx 0.6\sigma_1$. The use of median deviation for $\sigma = MAD$ also helps to effectively exclude the flaring states, which introduce non-Gaussian statistics and may not be relevant for the quasi-quietest state. For $n_1 \rightarrow \infty$ t-distribution approaches the normal distribution with the same error, though for simplicity we employ a normal distribution even at small n_1 . In summary, we are using a normal distribution with error equivalent to the median deviation of the observed sequence. This prescription cannot be improved upon or made exact, since we do not know the distribution function of the observed or the simulated quantities. This uncertainty also justifies the switch from a t-distribution to a normal distribution for the sequence.

As the number of observations, especially polarized, is small, the statistics of the observed sequence is not great. However, it is possible to synthesize a sequence of intensities on the top of several time shots for a limited volume in the parameter space and compute the typical statistics of the simulated sequence. We find that for the flux measurements with $n_1 > 5$ the observed error is about the simulated error $\sigma_{\text{obs}} \approx \sigma_{\text{sim}}$. This point will be elaborated elsewhere (Shcherbakov et al. 2010, in prep.). Thus, we can switch to the simulated error for any observables with low n_1 , assuming the typical statistics of the simulated sequence is representative of the entire parameter space. The combined observed/simulated median absolute deviations behave approximately in the following way. Flux error stays close to a constant $\sigma(F) = MAD(F) = 0.33$ Jy with ν , the CP error at 230 GHz and 349 GHz is about $\sigma(CP) = 0.27\%$. The linear polarization behaves differently. The ratio of error to the quantity stays approximately constant with frequency. Thus we are fitting for the logarithms of LP fractions with $\sigma(\log(LP)) = 0.26$. The combined errors are shown in Figure 1.

Next, we define χ^2 for flux fitting as

$$\chi_F^2 = \sum_{i=1}^7 \frac{(F_{i,\text{sim}} - F_{i,\text{obs}})^2}{\sigma(F)^2}, \quad (19)$$

for the set of 7 frequencies $\nu = 87, 102, 145, 230, 349, 680,$

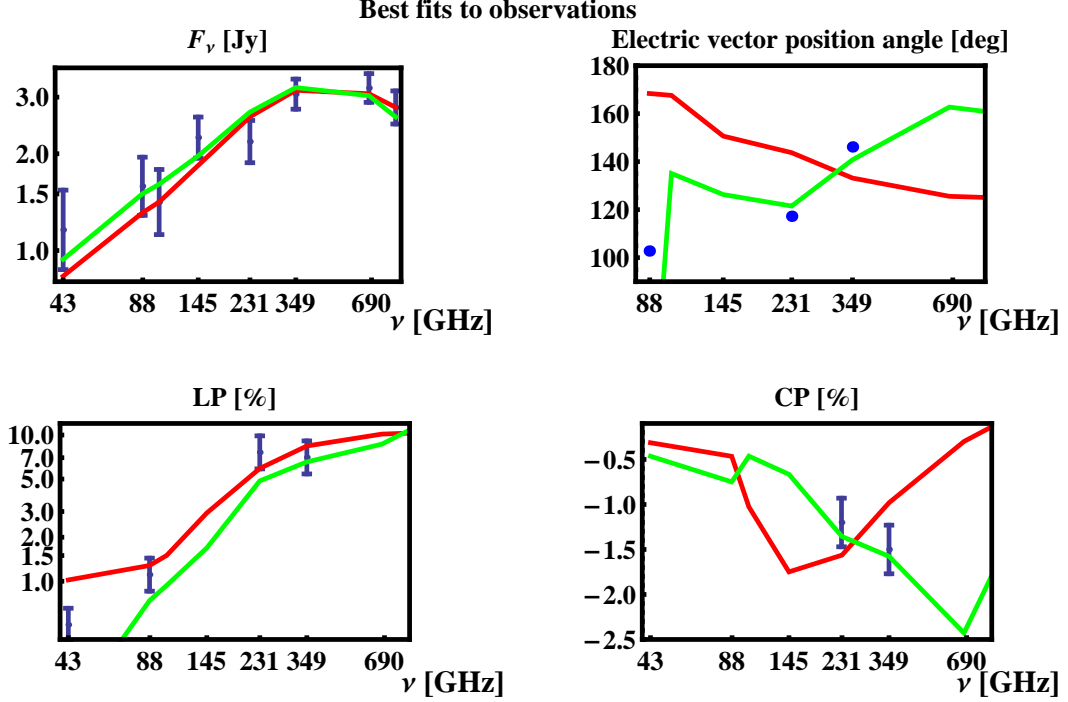


Figure 5. Fits to total flux (upper left panel), LP fraction (lower left), CP fraction (lower right), and EVPA angle (upper right) by the lowest χ^2 model for spin $a = 0.9$ (red/dark line) and the lowest χ^2 model for spin $a = 0.5$ (green/light line). Spin $a = 0.9$ model with $\chi^2 = 0.99$ has the inclination angle $\theta = 59^\circ$, the accretion rate $\dot{M} = 1.3 \cdot 10^{-8} M_\odot \text{year}^{-1}$, the ratio of temperatures $T_p/T_e = 23.5$ at $6M$, which corresponds to $T_e \approx 3.2 \cdot 10^{10}$ K at that distance from the BH in the equatorial plane. Spin $a = 0.5$ model with $\chi^2 = 0.84$ has $\theta = 70^\circ$, $\dot{M} = 7.0 \cdot 10^{-8} M_\odot \text{year}^{-1}$, and $T_p/T_e = 22$ at $6M$. The EVPA curves are arbitrarily shifted to approximate the EVPA at 300 GHz. External Faraday rotation measure helps to reconcile EVPA(230 GHz) and EVPA(349 GHz).

and 857 GHz. We add the LP at 87, 230, and 349 GHz and CP at 230 and 349 GHz for the full χ^2 :

$$\chi^2 = \chi_F^2 + \sum_{i=1}^3 \frac{(\log(LP_{i,\text{sim}}) - \log(LP_{i,\text{obs}}))^2}{\sigma(\log(LP))^2} + \sum_{i=1}^2 \frac{(CP_{i,\text{sim}} - CP_{i,\text{obs}})^2}{\sigma(CP)^2}. \quad (20)$$

The probability density is then

$$\rho(\chi^2|a, \theta, \dot{M}, C) = \exp\left(-\frac{\chi^2}{2}\right). \quad (21)$$

This is a function of spin, inclination angle, accretion rate, and heating constant. Now the search for minimum χ^2 is fully defined, but the integration over the parameter space requires priors, corresponding to functions that express the uncertainty about the probability density ρ before the data are taken into account (Berger 1985; Broderick et al. 2009). We expect no preferred spin orientation, which requires a uniform distribution over the solid angle and the prior $\pi(\theta) = \sin\theta$. The prior of spin a has more freedom. Broderick et al. (2009) assumed a uniform prior, however this may overestimate the importance of low spins. Gammie, Shapiro & McKinney (2004) showed that high spin BH $a \sim 0.9$ is quite a probable solution and $a = 0$ is not. It is then reasonable to substitute the integration over spin with some prior to a simple summation over spin for a set $a = 0, 0.5, 0.7, 0.9, 0.98$, favoring high spins. The heating parameter C is uncertain. The value $C = 0.33$ cited by Sharma et al. (2007)

was based on only a small part of total energy dissipation and may be unreliable. For our analysis we assume the uniform prior distribution of $\log C$. Such a prior gives equal probabilities for equal relative deviations $\Delta C/C$ near different points. Logarithmic prior is also the simplest possible assumptions as it has no free parameters. We explore the values of C from 0.15 to 0.75, which leads to T_p/T_e at $6M$ in between 6 and 80. All models fitting F_ν SED with $C = 0.15$ underpredict the linear polarization and all models with $C = 0.75$ overpredict the linear polarization, thus we cover all good models by using a wide range of C . For simplicity, the same prior is taken for the accretion rate \dot{M} : a uniform distribution in $\log \dot{M}$. A full analysis in the space of accretion rate \dot{M} is not possible due to limited computational resources. Instead, for each spin a , heating constant C , and inclination θ we find the best χ_F^2 for the values of flux F_ν (see eq.19) and explore the region close to the best fit. As the dependence of flux on accretion rate is uniform, this guarantees that we explore all regions with good full χ^2 defined by equation (20). Even if there is some good fit to LP and CP curves, but the flux values are either overpredicted or underpredicted, then the total χ^2 would be substantially larger than unity. The probability to have a certain spin is

$$P(a) = \iiint \rho(\chi^2|a, \theta, \dot{M}, C) \sin\theta d\theta \frac{dC}{C} \frac{d\dot{M}}{\dot{M}}. \quad (22)$$

The expectation value of any quantity Q is calculated as

the sum over spin as

$$\langle Q \rangle = \sum_a \iiint Q \rho(\chi^2 | a, \theta, \dot{M}, C) \sin \theta d\theta \frac{dC}{C} \frac{d\dot{M}}{\dot{M}}. \quad (23)$$

6. RESULTS

In the previous sections we described the observations, the numerical simulations of the dynamical structure, the polarized radiative transfer, and the statistical methods to compare the simulated spectra with the observations. Now we are ready to present the results of such a comparison, done for the first time for GR polarized radiative transfer over 3D GRMHD simulations. We are able to achieve $\chi^2 \sim 1$ fits to observations and find tight constraints on the expectation values of some quantities, whereas other quantities are still left poorly constrained.

Fits of polarized sub-mm observations of Sgr A* exhibit some ambiguity. Figure 5 shows the performance of two best fit models for different spins. The red (dark) curve corresponds to the best model for spin $a = 0.9$. It gives $\chi^2 = 0.99$ and has the inclination angle $\theta = 59^\circ$, the accretion rate $\dot{M} = 1.3 \cdot 10^{-8} M_\odot \text{year}^{-1}$, and the ratio of temperatures $T_p/T_e = 23.5$ at $6M$, which corresponds to $T_e = 3.15 \cdot 10^{10}$ K at that distance from the center in the equatorial plane. The green (light) curve on the same figure shows the best model for spin $a = 0.5$ with $\chi^2 = 0.84$ having $\theta = 70^\circ$, $\dot{M} = 7.0 \cdot 10^{-8} M_\odot \text{year}^{-1}$, and $T_p/T_e = 22$ at $6M$ with $T_e = 3.50 \cdot 10^{10}$ K. The performance of the models is similarly good. The upper left panel in Figure 5 shows the simulated curves of total flux with our effective error bars of observations. The spin $a = 0.5$ model has slightly larger flux at lower frequencies $\nu < 100$ GHz due to relatively more emission from the polar region, as compared to stronger emission from close to the BH for spin $a = 0.9$ model. However, the discrepancy is within the flux error. The LP fractions (lower left panel) are lower for spin $a = 0.5$ solutions, since at larger density the beam depolarization is larger due to larger Faraday rotation. The agreement of both curves with observations is fairly good. Whereas the behaviors of LP curves are qualitatively similar, the simulated CP fractions versus frequency ν (lower right panel) diverge between two fits. Both can reproduce the observed CP fractions at 230 GHz and 349 GHz. The goodness of fit is insignificantly better for spin $a = 0.5$, since both curves pass within 1.5σ errors from observations. However, the predictions for the peak CP are different: the spin $a = 0.5$ model predicts CP of $\approx -2.5\%$ at 700 GHz, whereas the spin $a = 0.9$ model predicts a peak CP of $\approx -1.7\%$ at 200 GHz, so that the observation of CP at 690 GHz would discriminate these two models. The fit to the EVPA angle is shown on the upper right panel. Whereas the slope of the spin $a = 0.5$ solution between 230 and 349 GHz is consistent with data, the slope of the $a = 0.9$ solution is not. Nevertheless, this should not put $a = 0.9$ spin model into disadvantage. The Faraday rotation effect, responsible for the slope of EVPA, depends strongly on the magnetic field strength $B(1000M)$ at distance $\sim 10^3 M$ from the BH. The increase of this poorly constrained magnetic field $B(1000M)$ can readily make up for the EVPA slope difference. Overall, both best-fitting models show good agreement with data, spin $a = 0.5$ model performing insignificantly better. Let us

now separate the physical effects responsible for the observed polarized quantities.

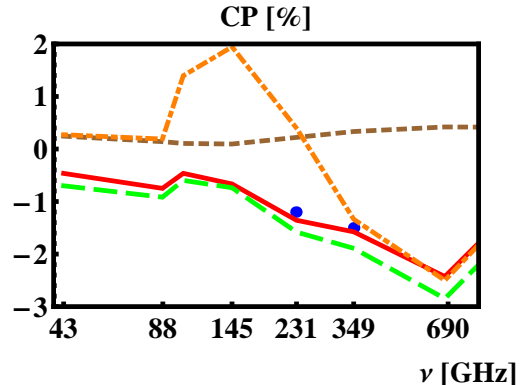


Figure 6. The contributions of different effects to CP fraction as functions of frequency for best-fitting $a = 0.5$ model. Observational points are blue, the best fit model is the solid line, the effect of Faraday conversion with zero V emissivity $\varepsilon_V = 0$ is the long-dashed line, the effect of V emissivity with zero Faraday conversion $\rho_Q = 0$ is the short-dashed line, the effect of Faraday conversion and emission without Faraday rotation $\rho_V = 0$ is the dot-dashed line. Emissivity in V mode contributes little to the observed CP. Surprisingly, CP does not change the sign as a function of frequency. The combined action of Faraday rotation and Faraday conversion takes places around 145 GHz, without Faraday rotation the sign of V changes.

Several (comparable in strength) radiative transfer effects may account for the observed polarized fluxes. Let us consider the production of circular polarization in the flow. Figure 6 shows the consequences of switching various physical effects off for the best fit model with spin $a = 0.5$. The solid curve is the result with all physics on. The long-dashed line below is produced, when circular emissivity is set to zero $\varepsilon_V = 0$. The short-dashed line corresponds to zero Faraday conversion $\rho_Q = 0$. The changes for the emissivity switched off are small, whereas setting Faraday conversion to zero leads to several times smaller CP of different sign, thus most of CP in this model is produced by Faraday conversion. It would be incorrect, however, to think that the simple linear to circular conversion explains the observed CP. The dot-dashed line in Figure 6 shows the CP fraction, when Faraday rotation is switched off ($\rho_V = 0$). The effect of Faraday rotation is insignificant at $\nu > 300$ GHz, but the rotation of the plane of linear polarization simultaneous with conversion between linear and circular polarizations produces a unique effect at lower ν . The expected sign oscillations of V with frequency do not happen, when Faraday rotation is also involved. The positive peak of CP at ~ 145 GHz, when $\rho_V = 0$, corresponds to only a small bump on the top of negative CP, when Faraday rotation is on. At even lower frequencies $\nu < 87$ GHz Faraday rotation helps to maintain relatively large levels of CP. Then, the LP fraction is close in the absolute value to the CP fraction. The spin $a = 0.9$ model exhibits qualitatively similar variations in CP.

The influence of Faraday rotation on LP fraction (left panel) and EVPA angle (right panel) is shown in Figure 7. The solid curves have all physics on and the dashed lines are computed for switched off Faraday rotation $\rho_V = 0$. The Faraday rotation is negligible at high frequencies and curves coincide at $\nu > 1$ THz. As the

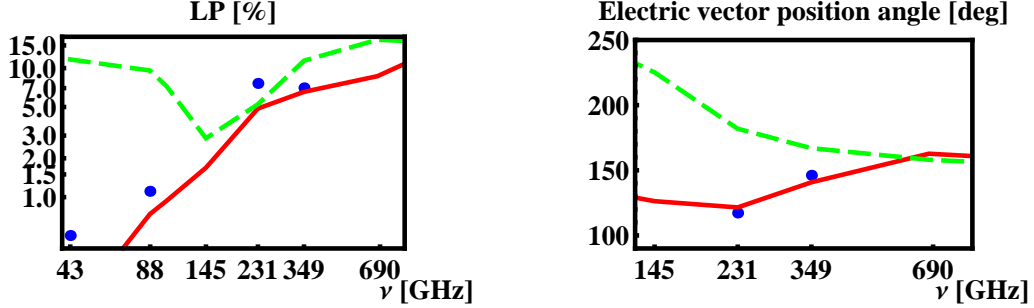


Figure 7. The contributions of different effects to LP fraction (on the left) and EVPA angle (on the right) for the best-fitting $a = 0.5$ model. The observational points are in blue, the best fit model is the solid line, the model without Faraday rotation $\rho_V = 0$ is the long-dashed line. Beam depolarization is weak without Faraday rotation and LP stays high at low frequencies. The change of the EVPA due to Faraday rotation is comparable to the difference of intrinsic emission EVPA, but has the opposite sign.

rotation of polarization plane is much stronger at low ν , a significant phase shift accumulates between different rays at the low end of the spectrum and cancellations of LP become strong at $\nu < 200$ GHz. Thus we illustrate the effect of beam depolarization (Bower et al. 1999a). The dip at 145 GHz is due to the first cancellation of LP, when there are two regions with close intensities and perpendicular EVPAs (Shcherbakov & Huang 2010). These cancellations can also make the LP fraction curve oscillatory (see fits in Huang et al. 2009a). In the absence of Faraday rotation the dependence of EVPA on frequency is not a constant line: the variations of intrinsic emitted EVPA are significant. Thus, the change of EVPA with ν should not always be ascribed to the effect of Faraday rotation. The positive slope of EVPA with ν , acquired due to negative Faraday rotation ρ_V , is comparable to the slope of intrinsic emitted EVPA.

The presence of two fits with largely different spins does not allow us to immediately decide on the value of BH spin. However, the study of models with parameters, close to the best-fitting parameters, may provide more information. If there is some coincidental cancellation in one of the models, then the close-by models have much higher χ^2 and such a best fit is excluded as accidental. On the Figure 8 we plot the contours of χ^2 near the best-fitting models for spin $a = 0.9$ (left column) and spin $a = 0.5$ (right column) in the space of ratio of temperatures T_p/T_e at $6M$ and accretion rate \dot{M} . The contours with $\chi^2 > 2$ are red (dark outer contours) and with $\chi^2 < 1$ are blue (dark central contours). The upper row shows χ_F^2 for the flux F_ν , whereas the lower row shows the full χ^2 . The plots of χ_F^2 (panels (a) and (c)) reveal significant degeneracy between the electron temperature and accretion rate: lower T_e and higher \dot{M} or higher T_e and lower \dot{M} both fit the flux quite well. The degeneracy breaks for the full χ^2 due to LP fitting, which fixes matter density. The well-fitting phase volume in the parameters of T_p/T_e and \dot{M} appears to be similar for both spins (panels (b) and (d)), thus none of the fits seems to be accidental. The impression changes, however, when the inclination angle θ is considered. In Figure 9 we plot the contours of χ^2 for the same models in the space of the ratio of temperatures T_p/T_e at $6M$ and spin inclination angle θ . First, note that the good fits for χ_F^2 (panels (a) and (c)) have almost constant electron temperature

T_e correspondent to a range of inclination angles θ . A much smaller range in θ is allowed according to the full χ^2 (panels (b) and (d)) with qualitatively different behavior for spin $a = 0.9$ and spin $a = 0.5$ solutions. In case of spin $a = 0.9$ on panel (b) the contours of χ^2 are smooth without significant cancellations, whereas the low χ^2 areas for spin $a = 0.5$ (panel (d)) constitute two regions with $\chi^2 \sim 10$ in between. Such a dependence for spin $a = 0.5$ points at accidental cancellations of LP fraction at certain θ undermines the significance of this fit. Similar conclusions can be drawn by comparing the total probabilities of spins.

In Figure 10 we show the total probability of spin $P(a)$ computed according to the equation (22). The upper red curves on both panels correspond to $P_F(a)$ based on flux-fitting χ_F^2 and the lower blue curves on both panels show $P(a)$ based on total χ^2 . The panel (a) shows $P_F(a)$ and $P(a)$ as functions of spin a . We see that the probability $P_F(a)$ is almost constant for a set of simulations with $a = 0.5, 0.7, 0.9, 0.98$, only slightly deviating for $a = 0$. The BH spin cannot be determined from fitting only the flux F_ν . When we include the polarized observations into fit, the situation significantly improves. The total probability curve peaks at spin $a = 0.9$, leaving only a $\sim 10\%$ chance for the spin $a = 0.5$ solutions and $< 1\%$ for the spin $a = 0$ solutions. Thus, only the spin $a = 0$ is reliably excluded based on quasi-quietest polarized sub-mm data and the most probable spin is $a = 0.9$. The result does not depend strongly on the prior of spin. The uniform prior spin $a = 0.5$ case still has 4 times lower probability compared to spin $a = 0.9$, and spin $a = 0$ is still reliably excluded. Usage of the averaged dynamical model raises an important question of reliability of results, that is whether the different averaging period would lead to vastly different probability. To test this possibility we compared the probabilities $P_F(a)$ and $P(a)$ for seven averaging periods of duration $860M$ in the range $14000 - 20000M$. The probability $P_F(a)$ stays almost constant, lowering only 8% for the last period compared to the first period suggesting that the simulations have reached a steady-state. The probability $P(a)$ shows variability by a factor of about 2 without a pronounced secular trend. High $P(a)$ may originate from favorable dynamical models with cancellations of LP over larger volume of parameter space.

There is another way to test the dynamical models

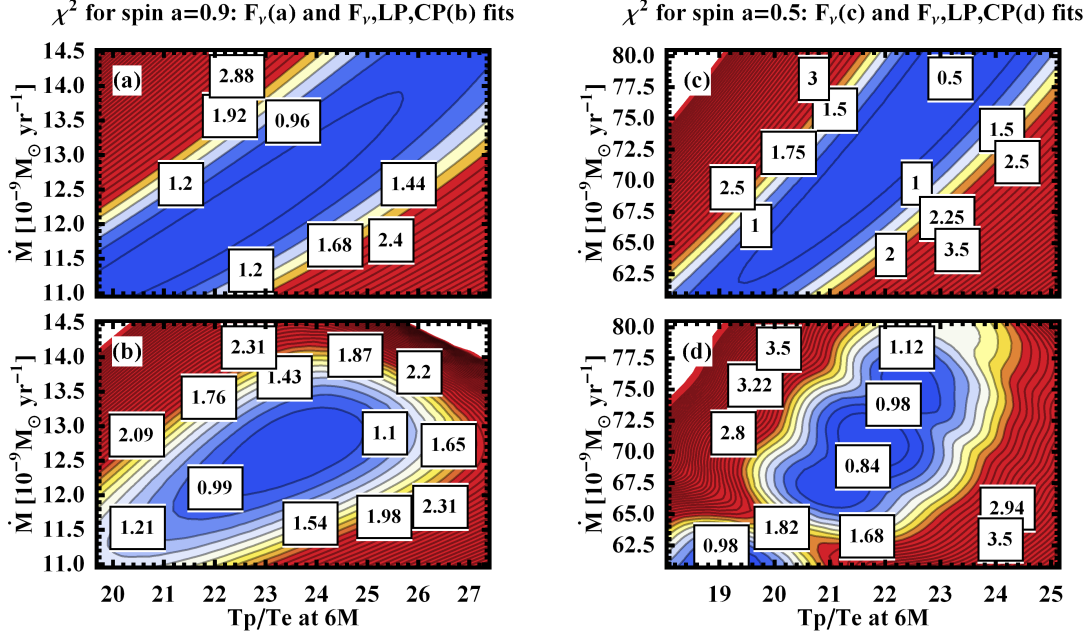


Figure 8. Behavior of χ^2 near the best-fitting models with spin $a = 0.9$ (left column) and spin $a = 0.5$ (right column) with changing accretion rate \dot{M} and ratio of temperatures T_p/T_e at $6M$. Contours of χ_F^2 for flux fitting are in the upper row, contours for full χ^2 are in the lower row.

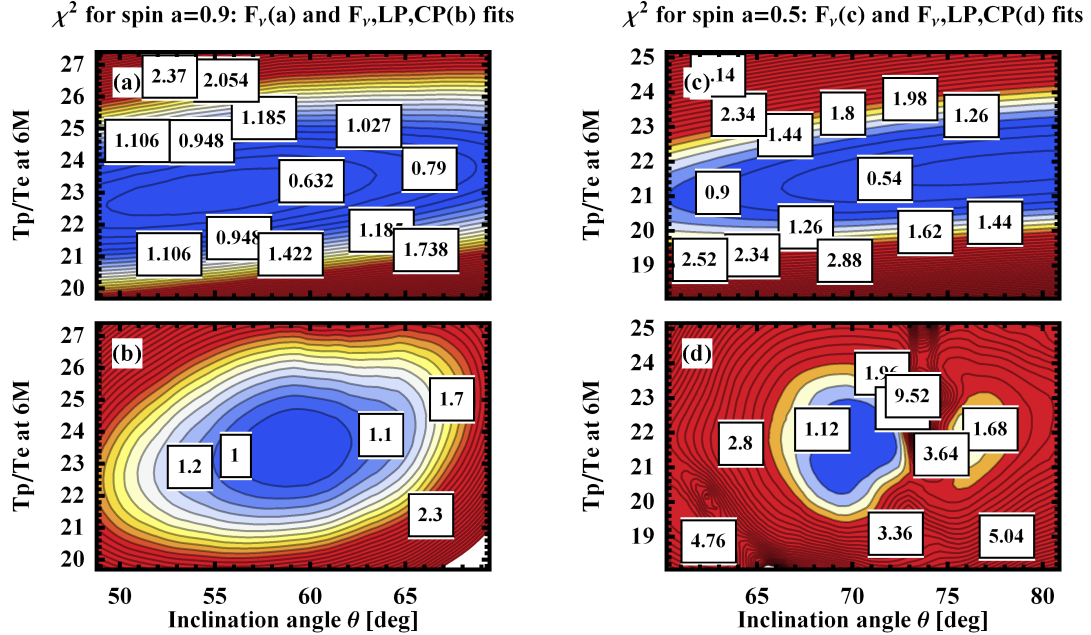


Figure 9. Behavior of χ^2 near the best-fitting models with spin $a = 0.9$ (left column) and spin $a = 0.5$ (right column) with changing ratio of temperatures T_p/T_e at $6M$ and inclination angle of BH spin θ . Contours of χ_F^2 for flux fitting are in the upper row, contours for full χ^2 are in the lower row.

against observations. The intrinsic image size was recently measured (Doeleman et al. 2008) with VLBI technique. It involved simultaneous measurement of flux $F = 2.4$ Jy at 230 GHz and correlated flux $F_{\text{corr}} \approx 0.35$ Jy at 3.5 G λ SMT-JCMT baseline. We plot the correlated flux with 3σ error bar in Figure 11 and compare that

with the simulated correlated fluxes, normalizing the total flux to 2.4 Jy. To simulate the correlated flux we follow Fish et al. (2009) and employ a Gaussian interstellar scattering ellipse with half-widths at half-maximum $7.0 \times 3.8G\lambda$ with position angle 170° east of north. We vary the position angle of BH spin and plot correlated

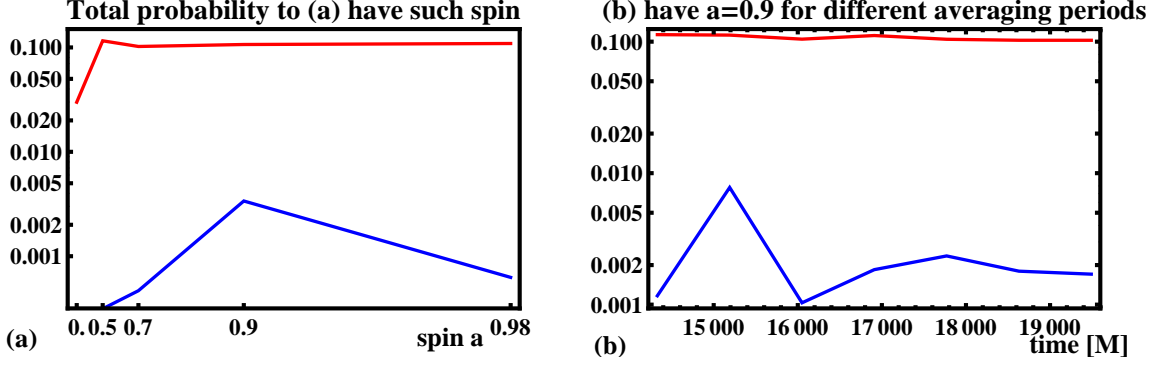


Figure 10. Probabilities for the BH to have a certain spin a , marginalized over the electron heating parameter C , inclination angle θ , and accretion rate \dot{M} . The red/upper curves correspond to the probability $P_F(a) = \langle \exp(-\chi^2(F)/2) \rangle$ of fitting the total flux at 7 frequencies. The blue/lower curve corresponds to the probability $P_{F,LP,CP}(a) = \langle \exp(-\chi^2(F,LP,CP)/2) \rangle$ of fitting the total flux at 7 frequencies, LP fraction at 3 frequencies and CP at 2 frequencies. Probabilities of spins $a = 0, 0.5, 0.7, 0.9, 0.98$ are shown on figure (a) for the model averaged over the period 14000 – 20000M. Spin $a = 0.9$ is marginally better than spins 0.7 and 0.98. Probabilities for spin $a = 0.9$ are shown on figure (b) for models averaged over smaller intervals within 14000 – 20000M range. Almost no secular drift is present for converged simulations.

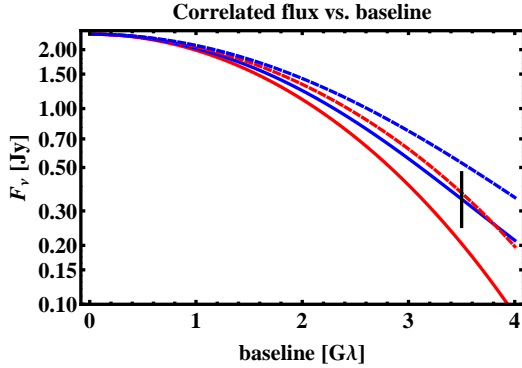


Figure 11. Correlated fluxes as functions of baseline normalized to 2.4 Jy total flux for best-fitting spin $a = 0.9$ model (dashed lines) and spin $a = 0.5$ model (solid lines). For each model the blue/upper line shows the smallest size (largest correlated flux) over all position angles of BH spin axis, the red/lower line shows the largest size (smallest correlated flux) over all position angles. The observation in Doeleman et al. (2008) with 3σ error bars at baseline 3.5 G λ is drawn for comparison.

flux curves with the largest (upper line) and the smallest (lower line) correlated flux at 3.5G λ . The correlated fluxes for both best-fitting models are shown: two dashed lines correspond to the spin $a = 0.9$ and two solid lines correspond to the spin $a = 0.5$. The spin $a = 0.9$ best-fitting model slightly overproduces the correlated flux, which indicates the size of the shadow is too small. In turn, the spin $a = 0.5$ best-fitting model slightly underproduces the correlated flux, indicating the size of the shadow is a bit too big. We discuss the possible ways to reconcile observations and simulations in the next section.

Having analyzed the best fits and compared all probabilities, we can calculate the expectation values of model parameters and constrain the BH spin orientation. Let us start with the inclination angle of BH spin θ ($\theta = 0^\circ$ for the face-on disk). On Figure 12 we plot the conditional probability densities $\rho(\theta|a)$ for inclination angle for the models with certain spin. This quantity is marginalized over the heating constant and accretion rate in a way similar to the equation (22). The probability density is not normalized, so the higher total area peaks correspond to the higher total probability of spin $P(a)$. Each peak

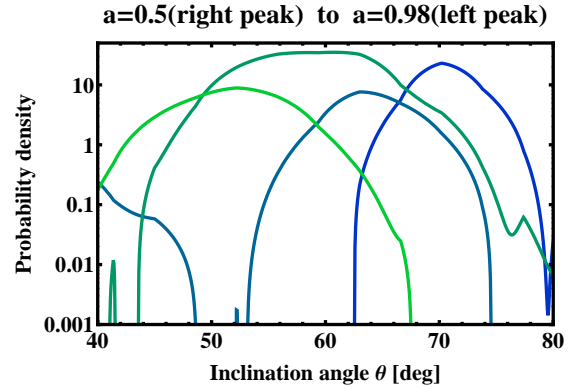


Figure 12. Marginalized over heating parameter C and accretion rate \dot{M} probability densities $\rho(\theta|a)$ of inclination angle θ . Each spin a is represented by a peak: $a = 0.5$ gives the rightmost peak, $a = 0.98$ gives the leftmost peak. The total areas under the curves are approximately proportional to total probabilities $P(a)$, thus the largest area for $a = 0.9$.

on the plot represents a separate value of spin: the rightmost peak for $a = 0.5$, then $a = 0.7$, next $a = 0.9$, and the leftmost peak for $a = 0.98$. The probable range of θ is quite small providing tight constraints on θ . The expectation value for inclination angle is $\theta = 59^\circ$ with a 90% confidence interval

$$\theta = 59^\circ \pm 9^\circ \quad (24)$$

marginalized over spin and θ according to the equation (23). Likewise, we can calculate the expectation value and the interval for electron temperature T_e at $6M$. The results are $T_e = 3.4 \cdot 10^{10}$ K for the expectation value and

$$T_e = 3.4_{-0.9}^{+1.2} \times 10^{10} \text{ K} \quad (25)$$

for 90% confidence interval. The best-fitting models give $T_e = 3.15 \cdot 10^{10}$ K for spin $a = 0.5$ model and $T_e = 3.50 \cdot 10^{10}$ K for spin $a = 0.9$ model. Unfortunately, the range of the accretion rate \dot{M} is too broad for the expectation value to correspond to a reasonable model. The ratio of the best-fitting accretion rates for the models with $a = 0.5$ and $a = 0.9$ is about $\dot{M}(0.5)/\dot{M}(0.9) \approx 5.5$, whereas the ratio of probabilities $P(0.9)/P(0.5) \approx 10$, so that the expectation value would be far from either fit.

Similarly, we do not compute the expectation value for spin a . When considering only the simulation with spin $a = 0.9$, we find the 90% confidence interval of accretion rate to be

$$\dot{M}(0.9) = 13_{-3}^{+4} \times 10^{-9} M_{\odot} \text{year}^{-1}. \quad (26)$$

There is one more quantity we can estimate: the position angle (PA) of the BH spin. Similarly to Huang et al. (2009a), we rely on intrinsic EVPA $\approx 117^{\circ}$ at 230 GHz and EVPA $\approx 146^{\circ}$ at 349 GHz as the median of observations (see § 2). For the model to fit the difference in EVPA, we add a Faraday rotation screen far from the BH with constant rotation measure (RM). Then we compute the required RM and the intrinsic PA to fit the simulated EVPAs at 230 and 349 GHz. The scattering of the PA from averaged simulations appears to be quite small. The best-fitting model with $a = 0.5$ gives PA = 101° east of north, whereas the best-fitting model with $a = 0.9$ needs PA = 96° . By marginalizing over spin, we obtain the expectation value PA = 96° and 90% confidence interval

$$\text{PA} = 96^{\circ} \pm 5^{\circ}. \quad (27)$$

While the error bars appear small, the real error bars are limited by observations. In fact, EVPA is a strongly variable quantity (Marrone et al. 2007) with fluctuations about $d\text{EVPA} \approx 20^{\circ}$, which places the effective 3σ error bar for the median PA at the level of $\pm 30^{\circ}$. Such a big range of PA precludes us from tightening the size estimates (see Figure 11) from the models. It is reasonable to employ the minimum and maximum correlated fluxes found over all orientations.

With known orientation of BH spin, we can plot the images in the black hole in the equatorial coordinates. Figure 13 shows images of total intensity I_{ν} for spin $a = 0.9$ best-fitting solution on upper left panel, for spin $a = 0.5$ best-fitting solution on lower left panel; CP intensity and LP intensity plots for spin $a = 0.9$ are shown on upper right and lower right, correspondingly. Blue (predominant) color on CP plot depicts the regions with negative CP intensity and red (subdominant) color depicts the regions with positive CP intensity. The total V flux from this solution is negative $V < 0$. The streamlines on LP plot are aligned with EVPA direction at each point. The spin axis is rotated by PA = 101° east of north for $a = 0.5$ solution and by PA = 96° for $a = 0.9$ solution. The spin axis is inclined at θ to the line of sight, so that the right (west) portions of the flow are closer to the observer. The color schemes for I_{ν} and LP plots are logarithmic: the brightest white is 20 times more intense than the darkest red. Negative logarithm and RGB black distinguish the dimmer part of the flow. The color scheme for CP plot is linear: white colors of both tints denote the regions with intensity about certain threshold, below the threshold the colors linearly fade to RGB black. By visually comparing the sizes of images with spin $a = 0.9$ and spin $a = 0.5$, one can arrive at the same conclusion as is drawn from Figure 11: size of $a = 0.9$ image is smaller at all orientations compared to the size of $a = 0.5$ image.

7. DISCUSSION AND CONCLUSIONS

Let us compare our results with estimates of Sgr A* accretion flow and BH parameters made by other groups.

Two separate searches for spin based on GR numerical simulations are reported so far: Moscibrodzka et al. (2009) and Dexter et al. (2010). The first paper browses the set of spins from $a = 0.5$ to 0.98 for 2D GRMHD simulations, fits X-Ray flux, 230 GHz flux, and slope at this frequency, and finds at least one model for each spin consistent with observations (see Table 3 therein). Their best-bet model has $a = 0.9$. Dexter et al. (2010) focuses on a set of 3D GRMHD, fits 230 GHz flux and size estimates and provides the table of spin probabilities with $a = 0.9$ again having the highest $P(a)$. Our results perfectly conform to the picture with the largest probability for $a = 0.9$, however the good fit with $a = 0.5$ is found. Thus, we are unable to provide narrow constraints on a , and neither do other groups. Some other spin estimates were done based on analytic models. Broderick et al. (2009) favor $a = 0$ solutions, Huang et al. (2009b) favor $a < 0.9$ in contradiction to less ad hoc simulation-based estimates, which emphasizes the importance of simulations. Another poorly constrained quantity is the accretion rate. Our two best fits have dramatically different $\dot{M} = 1.3 \cdot 10^{-8} M_{\odot} \text{year}^{-1}$ and $\dot{M} = 7.0 \cdot 10^{-8} M_{\odot} \text{year}^{-1}$. Drastically different \dot{M} are present in good models in Moscibrodzka et al. (2009) as well: $\dot{M} = 0.9 \cdot 10^{-8} M_{\odot} \text{year}^{-1}$ and $\dot{M} = 12 \cdot 10^{-8} M_{\odot} \text{year}^{-1}$ are found among good fits. Dexter et al. (2010) found relatively tight boundaries for 90% confidence interval of \dot{M} . This may reflect the true outcome of analysis as they used flow size as a constraint. The size of high \dot{M} /low a solutions can be substantially overpredicted. We do not incorporate size in χ^2 analysis, but if we assume a spin $a = 0.9$, then the conditional range of \dot{M} is quite narrow as well. Our range $\dot{M}(0.9) = 13_{-3}^{+4} \times 10^{-9} M_{\odot} \text{year}^{-1}$ is consistent with the full range $\dot{M} = 5_{-2}^{+15} \times 10^{-9} M_{\odot} \text{year}^{-1}$ (90%) in Dexter et al. (2010). Note, that Dexter et al. (2009) got much lower accretion rate $\dot{M}(0.9) = (1.0 - 2.3) \times 10^{-9} M_{\odot} \text{year}^{-1}$ as they assumed the equality of proton and electron temperatures $T_e = T_p$.

Unlike the spin and accretion rate, we can significantly constrain the ranges of inclination angle θ , electron temperature T_e at $6M$, and position angle PA. Out of all estimates in the literature, our 90% interval $\theta = 59^{\circ} \pm 9^{\circ}$ is the smallest, basically giving a single number for θ . This θ is consistent with the estimates $\theta = 50^{\circ}$ in (Broderick et al. 2009; Dexter et al. 2010). Huang et al. (2009a) and Huang et al. (2009b) favor slightly lower $\theta = 40^{\circ}, 45^{\circ}$, but have large error bars. Inclusion of polarized observations also puts stricter limits on T_e . Moscibrodzka et al. (2009) and Dexter et al. (2010) set constant T_p/T_e , whereas we and Huang et al. (2009a) calculate the profile of T_e . In all models, T_e is a shallow function of radius, which made Dexter et al. (2010) estimate the “common” $T_e = (5.4 \pm 3.0) \times 10^{10}$ K, which is the quantity calculated supposedly still at certain distance from the BH center. Setting this distance to $6M$ we arrive at consistent, but narrower range $T_e = 3.4_{-0.9}^{+1.2} \times 10^{10}$ K with 90% confidence. There are two kinds of constraints on BH spin position angle: 230 GHz correlated flux fitting and EVPA fitting. The first path was adopted in Broderick et al. (2009) and Dexter et al. (2010) with the results PA = $(-20^{\circ}) - (-70^{\circ})$. Surpris-

images of total and polarized intensities for best-fitting models

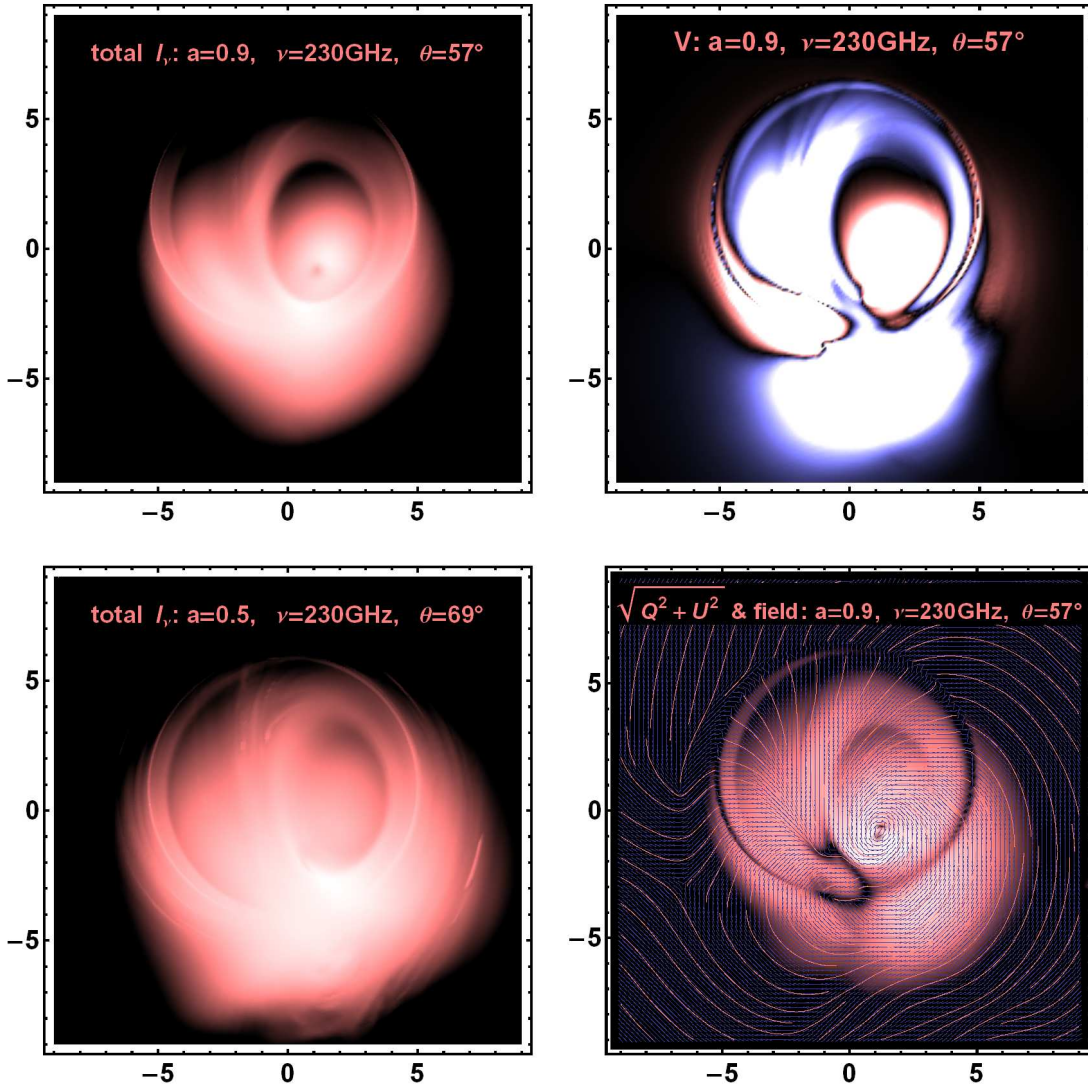


Figure 13. Images of polarized intensities for the best-fitting models: total intensity for spin $a = 0.5$ (lower left), total intensity for $a = 0.9$ (upper left), circular intensity for $a = 0.9$ (upper right), and linear intensity and streamlines along EVPA for $a = 0.9$ (lower right). Distances are in the units of the BH mass M . The images are rotated in the picture plane to fit the EVPA angle at 230 GHz. Brightest to darkest contrast is 20 on LP and I_{ν} images. CP is drawn in linear RGB colors: blue/dominant color is negative V, red/subdominant color is positive V. Ill-defined polar region does not contribute significantly to the emission.

ingly, these PA are inconsistent with polarization data. Meyer et al. (2007) predicts the range $\text{PA} = 60^\circ - 108^\circ$, whereas Huang gets either $\text{PA} \approx 115^\circ$ (Huang et al. 2009b) or $\text{PA} \approx 140^\circ$ (Huang et al. 2009a) depending on the model without calculating the range. Our estimate of $\text{PA} = 96^\circ \pm 30^\circ$ (with error bars from variability) is quite tight in turn and agrees well with Meyer et al. (2007). Significantly larger error bars, and the fact that only single-epoch size observations are available, make PA estimates from size less reliable than those from EVPA. In addition, the size of the flow may depend substantially on luminosity state (Broderick et al. 2009) or the presence of non-thermal structures, spiral waves, and other features.

In the present paper we combined several sophisticated techniques to arrive at our conclusions. Let us now examine the viability of the approaches employed. The

dynamical model, despite being state of the art, incorporates strong approximations. In spite of simulating several Keplerian orbits in the region within $25M$, the slopes of density n_e and temperatures T_p and T_e , fixed at the outer flow, break at a radius of roughly $25M$. This suggests one needs to simulate even larger domain in radius and potentially add other physical effects such as conduction (Johnson & Quataert 2007; Sharma et al. 2008; Shcherbakov & Baganoff 2010). The simulations with larger dynamical range also help to constrain the Faraday rotation, which happens for the present models partially outside of the simulated domain. The proper simulation of the polar region of the flow may be important as well. At present we artificially limit the magnetization and temperature there. If we do not, then the jet artifacts appear, similar to those in Moscibrodzka et al. (2009). The unanimous decision in favor of $a = 0.9$

spin for simulation-based models gives a hope the simulations of different groups are sufficiently similar and any simulation of the sort is representative. However, there are more caveats on the way. The convergence property of simulations does not mean their set converges to the right model, it is unclear if they possess the approximation property. For example, if the non-thermal electrons provide most of energy for sub-mm peak, then this may potentially invalidate the spin estimates (Shcherbakov & Huang 2010). Though the various heating prescriptions may not change the results significantly for thermal distribution. Electron temperature does not vary much in the emitting region, depreciating the difference of heating prescriptions.

The radiative transfer, in turn, has its own assumptions. Our emissivities in special synchrotron approximation are good enough, providing e.g. 2% agreement with exact emissivities (Leung, Gammie & Noble 2009; Shcherbakov & Huang 2010) for $B = 20$ G, $\theta_B = 1$ rad, $T_e = 6.9 \cdot 10^9$ K, and observed frequency $\nu = 100$ GHz. The agreement is better for larger T_e . The non-polarized radiative transfer of total intensity (Moscibrodzka et al. 2009; Dexter et al. 2010) has an intrinsic error in comparison with polarized radiative transfer with the same total emissivity ε_I , however the error is only 1 – 5%. We use the averaged dynamical model to calculate radiation and do not perform the statistical analysis of radiation from many simulation shots. This is a strong approximation, which cannot be easily justified and requires future improvement. Polarized radiative transfer appears to be much slower than unpolarized, and the present computation took 10k CPU-hours on a supercomputer to explore the full parameter space. Reliable statistics of radiation over many time shots may require up to 1M CPU-hours, and is not viable at present.

There are still unaccounted sources of error. The mass of the BH in the Galactic Center is known to within 10% (Ghez et al. 2008) and the distance is known to 5%. We do not perform a detailed analysis here, but it seems that these uncertainties would not lead to significant changes in our predictions. A simple shift to slightly lower spin should be able to mimic the effect of smaller BH or a BH at larger distance from us.

Apart from questions of modeling, the improvement of observational data can lead to further insights on the flow structure and more reliable estimates of BH spin. The detailed comparison of flux, LP, and CP curves in Figure 5 show that the models with spin $a = 0.5$ and spin $a = 0.9$ have discrepancies in the regions, not constrained by observations. In particular, the CP fractions at 145 and 690 GHz are different. At latter frequency the values -0.3% versus -2.5% are found and observations with SMA should help discriminating between two spins. The EVPA data needs improvement as well. Despite some statistics is available at 230 GHz and 349 GHz, the variability of EVPA is about 20° , which translates into 30° (3σ) uncertainty of PA, whereas the modeling uncertainty is only several degrees. More observations of EVPA at these frequencies will help to find the Faraday rotation measure more precisely and constraint the PA of BH spin. An alternative is to observe at higher frequencies $\nu \geq 690$ GHz, where both Faraday rotation effect and fluctuations of intrinsic emission EVPA are

small. Another important quantity is LP at 87 GHz, whose statistics consists of only 2 papers with short observations. Variations in simulated LP(87GHz) is the main reason for wiggles of χ^2 near the best fit for spin $a = 0.5$ (see lower-right panels in Figure 8 and Figure 9). Refinement of the observed median LP(87GHz) could potentially help discriminate between $a = 0.5$ and $a = 0.9$ spin solutions: its current median lies between the predictions of these two models (see lower-left panel in Figure 5). A measurement of the emitting region size or correlated flux is also promising. Despite the correlated flux at 230 GHz being measured at the SMT-JCMT 3.5G λ baseline, the statistics of this measurement are needed to capture variations of F_{corr} over at least a year to be comparable with the statistics of total flux. The correlated flux at this baseline is exponentially sensitive to the physical flow size, which can make slightly brighter states have significantly lower F_{corr} . As a caveat, the conclusion on image sizes may depend on behavior of matter in the ill-defined polar regions. Our models do not exhibit significant emission from high latitudes at 230 GHz (see Figure 13) or anywhere above 87 GHz.

The present paper offers substantial improvement of the previous estimates of Sgr A* spin value and orientation and accretion flow properties. Though there is significant room for improvement. The future work would incorporate more statistics from recent polarized observations in sub-mm. Future 3D GRMHD simulations would have higher dynamical range converging to $r > 50M$ and likely have a more pronounced outflow. Adding Comptonization to radiative transfer would allow testing the quiescent X-rays luminosity $L \approx 4 \cdot 10^{32} \text{erg s}^{-1}$ within 2 – 10 keV (Shcherbakov & Baganoff 2010). So far we focused on quasi-quiescent state and discarded the information of simultaneity. These data will be used in future analysis of observations to tighten the error bars. The time variability properties can be found from the simulations and compared to the observed ones. In particular, the “jet lags” (Yusef-Zadeh et al. 2008; Maitra, Markoff & Falcke 2009) and tentative QPOs (Genzel et al. 2003; Eckart et al. 2006; Miyoshi 2010) should be investigated using the simulations.

8. ACKNOWLEDGEMENTS

The authors are grateful to Lei Huang for checking various emissivity prescriptions, to Ramesh Narayan for extensive discussions and comments, to Avi Loeb, Avery Broderick, James Moran, Steven Cranmer for useful comments. The numerical simulations and the radiative transfer calculations in this paper were partially run on the Odyssey cluster supported by the FAS Sciences Division Research Computing Group and were partially supported by NSF through TeraGrid resources provided by NCSA (Abe), LONI (QueenBee), and NICS (Kraken) under grant numbers TG-AST080025N and TG-AST080026N. The paper is partially supported by NASA grants NNX08AX04H (RVS&Ramesh Narayan), NNX08AH32G (Ramesh Narayan), NSF Graduate Research Fellowship (RFP), and NASA Chandra Fellowship PF7-80048 (JCM).

REFERENCES

- Aitken, D. K., Greaves, J., Chrysostomou, A., Jenness, T., Holland, W., Hough, J. H., Pierce-Price, D., Richer, J. 2000, *ApJ*, 534, 173
- An, T., Goss, W. M., Zhao, J.-H., Hong, X. Y., Roy, S., Rao, A. P., Shen, Z.-Q. 2005, *ApJ*, 634, 49
- Baganoff, F. K., et al. 2003, *ApJ*, 591, 891
- Berger, J. O. 1985, "Statistical Decision Theory and Bayesian Analysis", (New York: Springer-Verlag)
- Blandford, R. D., & Begelman, M. C. 1999, *MNRAS*, 303L, 1
- Bower, G. C., Falcke, H., Backer, D. C. 1999a, *ApJ*, 523, L29
- Bower, G. C., Wright, M. C. H., Backer, D. C., Falcke, H. 1999b, *ApJ*, 527, 851
- Bower, G. C., Wright, M. C. H., Falcke, H., Backer, D. C. 2001, *ApJ*, 555, 103
- Bower, G. C., Falcke, H., Sault, R. J., Backer, D. C. 2002, *ApJ*, 571, 843
- Bower, G. C., Wright, M. C. H., Falcke, H., Backer, D. C. 2003, *ApJ*, 588, 331
- Bower, G. C., Falcke, H., Wright, M. C., Backer, & Donald C. 2005, *ApJ*, 618, 29
- Broderick, A. E., Fish, V. L., Doeleman, S. S., Loeb, A. 2009, *ApJ*, 697, 45
- Chan, C.-K., Liu, S., Fryer, C. L., Psaltis, D., O'zel, F., Rockefeller, G., Melia, Fulvio 2009, *ApJ*, 701, 521
- De Villiers J.-P., Hawley J. F., Krolik J. H., 2003, *ApJ*, 599, 1238
- Dexter, J., Agol, E., Fragile, P. C. 2009, *ApJ*, 703, 142
- Dexter, J., Agol, E., Fragile, P. C., McKinney, J. C. 2010, *ApJ*, 717, 1092
- Dolence, J. C., Gammie, C. F., Moscibrodzka, M., Leung, P. K. 2009, *ApJS*, 184, 387
- Doeleman S. S. et al 2001, *AJ*, 121, 2610
- Doeleman, S. S. et al. 2008, *Nature*, 455, 78
- Eckart, A., Schödel, R., Meyer, L., Trippe, S., Ott, T., Genzel, R. 2006, *A&A*, 455, 1
- Falcke, H., Goss, W. M., Matsuo, H., Teuben, P., Zhao, J.-H., Zylka, R. 1998, *ApJ*, 499, 731
- Fish, V. L., Broderick, A. E., Doeleman, S. S., Loeb, A. 2009, *ApJ*, 692, L14
- Fuerst, S. V., Wu, K. 2004, *A&A*, 424, 733
- Gammie, C. F., McKinney, J. C., Toth, G. 2003, *ApJ*, 589, 444
- Gammie, C. F., Shapiro, S. L., McKinney, J. C. 2004, *ApJ*, 602, 312
- Gammie, C. F., Leung, P. K. 2010, *MNRAS*, submitted
- Ghez, A. M., et al. 2008, *ApJ*, 689, 1044
- Ghosh, S., & Mukhopadhyay, B. 2007, *ApJ*, 667, 367
- Genzel, R., Schödel, R., Ott, T., Eckart, A., Alexander, T., Lacombe, F., Rouan, D., Aschenbach B. 2003, *Nature*, 425, 934
- Goldston, J. E., Quataert, E., Igumenshchev, I. V. 2005, *ApJ*, 621, 785
- Hamaker J. P., Bregman J. D., 1996, *A & AS*, 117, 161
- Herrnstein, R. M., Zhao, J.-H., Bower, G. C., Goss, W. M. 2004, *AJ*, 127, 3399
- Huang, L., Liu, S., Shen, Z.-Q., Cai, M. J., Li, H., & Fryer, C. L. 2008, *ApJ*, 676L, 119
- Huang, L., Liu, S., Shen, Z.-Q., Yuan, Y.-F., Cai, M. J., Li, H., & Fryer, C. L. 2009a, *ApJ*, 703, 557
- Huang, L., Takahashi, R., Shen, Z.-Q. 2009b, *ApJ*, 706, 960
- Igumenshchev, I. V. 2008, *ApJ*, 677, 317
- Johnson, B. M., Quataert, E. 2007, *ApJ*, 660, 1273
- Krichbaum T. P. 1998, *A&A*, 335, L106
- Krichbaum, T. P., Graham, D. A., Bremer, M., Alef, W., Witzel, A., Zensus, J. A., Eckart, A. 2006, *JPhCS*, 54, 328
- Legg, M. P. C., Westfold, K. C., 1968, *ApJ*, 154, 499
- Leung, P. K., Gammie, C. F., Noble S. C. 2009, *ApJ*, submitted
- Li, J., Shen, Z.-Q., Miyazaki, A., Huang, L., Sault, R. J., Miyoshi, M., Tsuboi, M., Tsutsumi, T. 2008, *JPhCS*, 131, 2007
- Lo, K. Y., Shen, Z.-Q., Zhao, J.-H., Ho, P. T. P. 1998, *ApJ*, 508, L61
- Lu, R.-S., Krichbaum, T. P., Eckart, A., König, S., Kunneriath, D., Witzel, G., Witzel, A., Zensus, J. A. 2008, *JPhCS*, 131, 2059
- Macquart, J.-P., Bower, G. C., Wright, M. C. H., Backer, Donald C., Falcke, H. 2006, *ApJ*, 646, L111
- Mahadevan, R. 1998, *Nature*, 394, 651
- Maitra, D., Markoff, S., Falcke, H. 2009, *A&A*, 508, 13
- Marrone, D. P., Moran, J. M., Zhao, J.-H., Rao, R. 2006a, *JPhCS*, 54, 354
- Marrone, D. P., Moran, J. M., Zhao, J.-H., Rao, R. 2006b, *ApJ*, 640, 308
- Marrone, D. P., Moran, J. M., Zhao, J., & Rao R., 2007, *ApJ*, 654L, 57
- Marrone D. P., et al. 2008, *ApJ*, 682, 373
- Mauerhan, J. C., Morris, M., Walter, F., Baganoff, F. K. 2005, *ApJ*, 623, 25
- McKinney, J. C., & Gammie, C. F. 2004, *ApJ*, 611, 977
- McKinney, J. C. 2006, *MNRAS*, 368, 1561
- McKinney, J. C., & Blandford, R. D. 2009, *MNRAS*, 394, L126
- Melrose, D. B. 1971, *Ap&SS*, 12, 172
- Meyer, L., Schödel, R., Eckart, A., Duschl, W. J., Karas, V., Dovčiak, M. 2007, *A&A*, 473, 707
- Miyazaki, A., Tsutsumi, T., Tsuboi, M. 2004, *ApJ*, 611, 97
- Miyoshi, M., Shen, Z.-Q., Oyama, T., Takahashi, R., Kato, Y. 2010, *astro-ph/0906.5511*
- Moscibrodzka, M., Gammie, C. F., Dolence, J. C., Shiokawa, H., Leung, P. K. 2009 *ApJ*, 706, 497
- Munoz, D., Marrone, D., Moran, J. 2009, *Bulletin of the AAS*, 41, 761
- Narayan, R., & Yi, I. 1995, *ApJ*, 452, 710
- Narayan, R., Yi, I., Mahadevan, R. 1995, *Nature*, 374, 623
- Narayan, R., Mahadevan, R., Grindlay, J. E., Popham, R. G., Gammie, C. 1998, *ApJ*, 492, 554
- Özel, F., Psaltis, D., Narayan, R. 2000, *ApJ*, 541, 234
- Pacholczyk, A. G. 1970, "Radio astrophysics. Nonthermal processes in galactic and extragalactic sources", (Freeman: San Francisco)
- Penna, R. F., McKinney, J. C., Narayan, R., Tchekhovskoy, A., Shafee, R., McClintock, J. E. 2010, *ApJ*, accepted
- Rybicki, G. B., & Lightman, A. P. 1979, "Radiative processes in astrophysics." (Wiley-Interscience: New York)
- Sazonov, V. N. 1969, *Soviet Astronomy*, 13, 396
- Serabyn, E., Carlstrom, J., Lay, O., Lis, D. C., Hunter, T. R., Lacy, J. H. 1997, *ApJ*, 490, L77
- Shafee R., McKinney J. C., Narayan R., Tchekhovskoy A., Gammie C. F., McClintock J. E., 2008, *ApJ*, 687, L25
- Sharma, P., Quataert, E., Hammett, G. W., & Stone, J. M. 2007, *ApJ*, 667, 714
- Sharma, P., Quataert, E., Stone, J. M. 2008, *MNRAS*, 389, 1815
- Shcherbakov, R. V. 2008, *ApJ*, 688, 695
- Shcherbakov, R. V., Baganoff F. K. 2010, *ApJ*, 716, 504
- Shcherbakov, R. V., Huang, L. 2010, *MNRAS*, submitted
- Shen, Z.-Q., Lo, K. Y., Liang, M.-C., Ho, P. T. P., Zhao, J.-H. 2005, *Nature*, 438, 62
- Shkarofsky, I. P., Johnston, T. W., Bachynski, M. P. 1966, "The particle kinetics of plasma," (Addison-Wesley Publishing Company: London)
- Yuan, F., Markoff, S., & Falcke, H. 2003, *ANS*, 324, 453
- Yuan, F., Quataert, E., Narayan, R. 2004, *ApJ*, 606, 894
- Yusef-Zadeh, F., Wardle, M., Cotton, W. D., Heinke, C. O., Roberts, D. A. 2007, *ApJ*, 668, 47
- Yusef-Zadeh, F., Wardle, M., Heinke, C., Dowell, C. D., Roberts, D., Baganoff, F. K., Cotton, W. 2008, *ApJ*, 682, 361
- Yusef-Zadeh, F. et al. 2009, *ApJ*, 706, 348
- Zhao, J.-H., Young, K. H., Herrnstein, R. M., Ho, P. T. P., Tsutsumi, T., Lo, K. Y., Goss, W. M., Bower, G. C. 2003, *ApJ*, 586, 29